

Intrinsic properties of suspended MoS₂ on SiO₂/Si pillar arrays for nanomechanics and optics.

Julien Chaste^{1*}, Amine Missaoui¹, Si Huang¹, Hugo Henck¹, Zeineb Ben Aziza¹, Laurence Ferlazzo¹, Carl Naylor², Adrian Balan², Alan. T. Charlie Johnson Jr.², Rémy Braive^{1,3}, Abdelkarim Ouerghi¹

¹ Centre de Nanosciences et de Nanotechnologies, CNRS, Univ. Paris-Sud, Université Paris-Saclay, C2N – Marcoussis

²Department of Physics and Astronomy, University of Pennsylvania, 209S 33rd Street, Philadelphia, Pennsylvania 19104 6396, United States

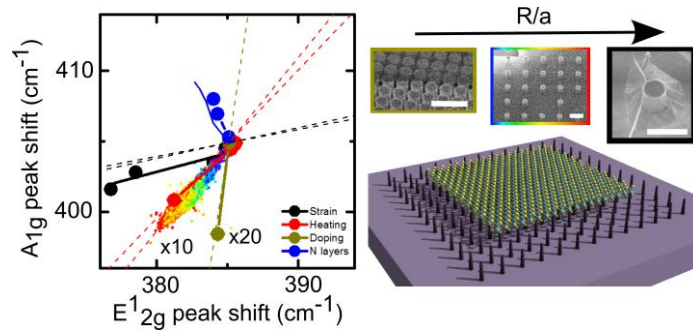
³Université Paris Diderot, Sorbonne Paris Cité, 75207 Paris Cedex 13, France

* Corresponding author: julien.chaste@c2n.upsaclay.fr

Abstract

Semiconducting 2D materials, such as transition metal dichalcogenides (TMDs), are emerging in nanomechanics, optoelectronics, and thermal transport. In each of these fields, perfect control over 2D material properties including strain, doping, and heating is necessary, especially on the nanoscale. Here, we study clean devices consisting of membranes of single-layer MoS₂ suspended on pillar arrays. Using Raman and photoluminescence spectroscopy, we have been able to extract, separate and simulate the different contributions on the nanoscale and to correlate these to the pillar array design. This control has been used to design a periodic MoS₂ mechanical membrane with a high reproducibility and to perform optomechanical measurements on arrays of similar resonators with a high-quality factor of 600 at ambient temperature, hence opening the way to multi-resonator applications with 2D materials. At the same time, this study constitutes a reference for the future development of well-controlled optical emissions within 2D materials on periodic arrays with reproducible behavior. We measured a strong reduction of the MoS₂ band-gap induced by the strain generated from the pillars. A transition from direct to indirect band gap was observed in isolated tent structures made of MoS₂ and pinched by a pillar. In fully suspended devices, simulations were performed allowing both the extraction of the thermal conductance and doping of the layer. Using the correlation between the influences of strain and doping on the MoS₂ Raman spectrum, we have developed a simple, elegant method to extract the local strain in suspended and non-suspended parts of a membrane. This opens the way to experimenting with tunable coupling between light emission and vibration.

KEYWORDS: 2D materials, suspended membranes, Raman spectroscopy, Strain, band gap transition, optomechanics



Bi-dimensional (2D) materials (such as graphene, transition metal dichalcogenides (TMDs) *e.g.* MoS₂ and WSe₂) are representative of ‘flatland’ technology. Due to the 2D nature of these materials, their intrinsic properties are greatly influenced by the surrounding environment on the nanoscale. Within these systems, the suspended structures^{1–3} are hybrid systems with transport performance,^{4–9} tunable optoelectronics behavior^{10–14} and nanomechanical properties^{15–17} that are all interesting on their own, but which can be coupled together, for example, the coupling of a vibration with a localized quantum emitter. Only a few systems at the interface between nanomechanics and nano-optics have achieved a similar richness of possibilities.^{18,19} Control over strain, doping, and temperature in 2D materials is vital for both the nanomechanical performance and the localized optical emission. Achieving such control is directly related to sample quality and to local nanostructuring of the suspended membranes.

Up to now, the experimental realization of suspended nanomechanical resonators has focused mainly on multilayer MoS₂^{15–17,20–22} without specific nanostructuring and with single resonator systems. Nevertheless, in order to achieve the next step in the engineering of 2D structures, it is necessary to combine high-quality 2D membranes with a controlled nanostructuring process.

In parallel, localized quantum dots and efficient quantum emitters made by strain nano-engineering of TMDs^{11–14} have been measured using peak arrays on a substrate for non-suspended 2D materials. TMDs are suitable materials for such optical applications because of their semiconducting properties with different band gap energies and the possibility to finely tune their doping. They can also be easily combined to form interesting heterostructures with various properties. When a TMD membrane is distorted by nanopillars, the strain will strongly influence the band structure and hence allow the creation of confined modes for electronics and optics (typically, 1% of strain reduces the band gap by about 0.1 eV).^{23,24} Specifically, in suspended samples, static strain and band structure can be tuned by applying an electrostatic potential using an embedded back gate. Such a design, consisting of a membrane suspended on nanopillars, represents a platform for the creation of highly efficient and tunable optoelectronic devices. Nonetheless, a good understanding and control of the strain, doping, and temperature on the nanoscale are essential. In particular, it is fundamental to understand the mechanism of the direct to indirect bandgap transition in monolayer TMDs under strain. Here we use suspended membranes on nanopillar arrays to elucidate these aspects. Although MoS₂ is subjected to a small broadening of its emission peaks, it has distinct Raman features in contrast to WSe₂. Moreover, MoS₂ has greater resistance to oxidation and is a referenced material among the TMDs, especially for Raman spectroscopy, nanomechanics, nanostructuring by nanopillars and photovoltaic^{23,24} or photocurrent generation.²⁵

Here, we study a system composed of suspended MoS₂ membranes deposited on nanopillar arrays in order to find a correlation between nanostructure dimension and strain, doping and temperature variations. We use a device with a monolayer deposited directly on top of SiO₂/Si nanopillar arrays acting as a “flying carpet”, where the MoS₂ layer itself consists of suspended and non-suspended parts.

Results

Thanks to chemical vapor deposition, very large 2D membranes (>100µm) of monolayer MoS₂ were used. We systematically studied the effect of pillar geometry on the strain, doping, and heating of the MoS₂ flakes by Raman spectroscopy and photoluminescence. We noted that, in some parts of the sample, periodic ripples, linked to pillar position, had been created in the MoS₂ flakes. The effect of these ripples was correlated to a strain effect in the Raman spectra.

In order to strongly enhance this strain effect, we spatially separated the pillars. In this configuration, it was possible to obtain a “tent” structure around one or more nanopillars. The 2D membrane sat on the tops of the pillars, thus creating a high strain gradient along the tent. This makes the structures suitable for obtaining a strong piezo-phototronic effect in 2D materials and gives rise to artificial atomic states within the 2D membranes.²⁴ We have also observed with Raman spectroscopy, the appearance of indirect band gaps induced by high strain and nanostructuring in monolayer MoS₂. We managed to optically separate strain, heating and doping effects using Raman spectroscopy and to control these by varying the device geometry itself. Clear evidence of a correlation was highlighted between the observed behavior and the aspect ratio R/a (where R is the peak radius and a, the peak separation length).

A suspended monolayer of MoS₂ (triangle shaped) over a large array of SiO₂ pillars is shown in the diagram in Figure 1. The sample was made using a method similar to Reserbat-Plantey *et al.*,²⁶ with doped Si/SiO₂ as substrate. The pillar mask was made using e-beam lithography, followed by Ni deposition. The pillars were formed using dry etching of the SiO₂/Si substrate before MoS₂ deposition and the Ni mask was completely removed afterward by wet etching. Two different samples were measured, labeled A and B, respectively, with SiO₂ thicknesses of 1450 nm and 670 nm, respectively. The pillar heights were 820 nm for sample A and 420 nm for sample B. In sample B, the optical reflection at 532 nm of the MoS₂-substrate cavity was optimized (see SI).²⁷ Large monodomains of MoS₂ were grown by chemical vapor deposition (CVD) on a non-patterned Si/SiO₂ substrate and then transferred to the pillar arrays by wet transfer, as described in previous studies,^{28,29} After a few cycles of cleaning in water, the MoS₂-PMMA was transferred on top of the pillar substrate, the resist dissolved in acetone and the sample dried in a critical point dryer. The results with different R/a ratios are presented in Figures 1 and SI. Using this technique, we managed to obtain large membranes (about 6.5 µm long) of fully suspended MoS₂, as shown in Figure 1c.

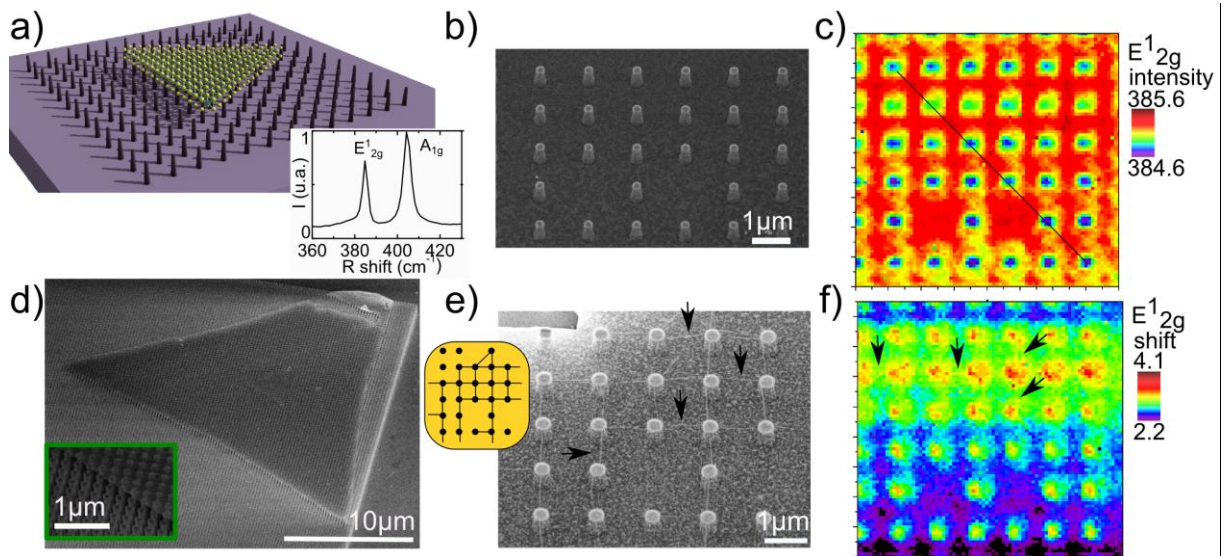


Figure 1: MoS₂ on nanopillar arrays: a) Diagram of a suspended MoS₂ layer deposited over a SiO₂ pillar array and inset showing a typical Raman spectrum with the E¹_{2g} and A_{1g} peaks in the suspended region. b),d) and e) E-beam image of typical flakes of MoS₂ fully suspended over pillar arrays. In e), lines and ripples at specific positions correlate with the pillar array pattern, as also seen in the inset for clarity. In this area, the ripple number is close to covering 100% of the surface. In c) and f), Raman mapping of the E¹_{2g} peak position shift and intensity along the SiO₂ peak array are shown. Periodic patterns are seen in correlation with the SiO₂ peak position. The arrows in f) highlight some lines in the peak position of E¹_{2g} mapping relying on the different pillars and attributed to similar ripples and strain patterns as in e). These lines are not visible in the peak position of A_{1g}.

In Figure 1, organized ripples can be seen clearly connecting the peak apices in the suspended membrane that appear in some regions of the samples. Completely planar features were also obtained. Generally, the organized ripples appeared preferentially at the borders of the MoS₂ flakes, while the central areas stayed relatively flat. These ripples were also observed in the case of non-suspended graphene deposited on similar pillar surfaces.²⁶ These ripples originated from the stress created at the peak apex and distributed along the membrane.²⁶ In fact, the model of these mechanical instabilities can be described by a suspended Föppl-Hencky membrane with a clamped boundary condition and submitted to a point load.^{24,30} This is a good indication that strain control on the nanoscale is possible with peak array engineering.

Hereafter, the Raman measurements obtained at ambient conditions on SiO₂ pillar arrays fully covered by a very clean and uniformly suspended monolayer MoS₂ membrane are presented and discussed. The main apparent feature is correlated to pillar patterns in both peak intensity and position: there are physical contact and interaction between the MoS₂ and the top of the pillars. We identified a strain signature along the ripple positions in the MoS₂ Raman maps of the E¹_{2g} mode (Figure 1e). This effect was absent in the A_{1g} peak position. In order to determine the strain at the pillar apex, where it must be of maximum amplitude, the contributions from doping, heating, and strain had to be separated. To do so, one identified the Raman dependency of each contribution; here we propose another possibility by engineering high strain in a tent-like structure.

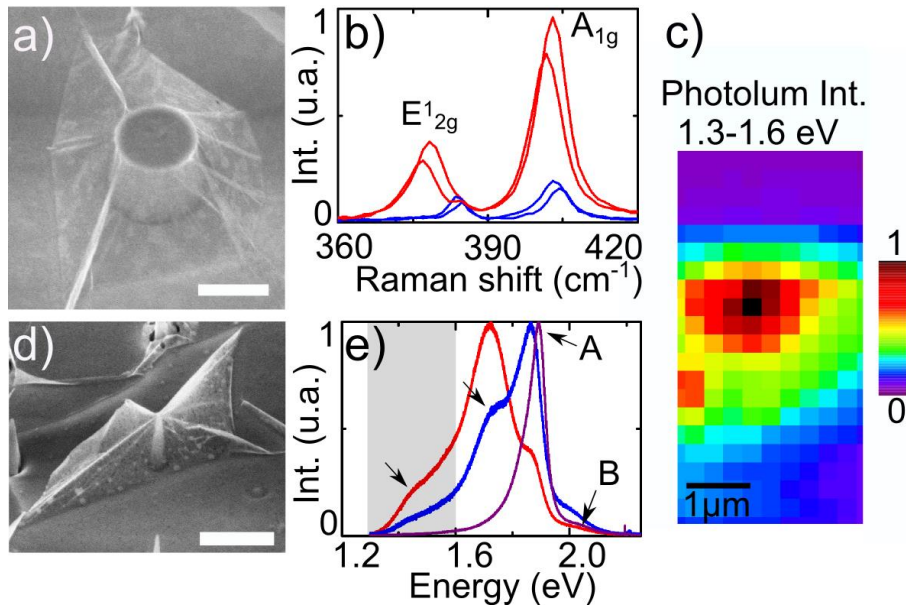


Figure 2: Strain engineering with C2N samples: a) and b) A “tent” structure made of CVD MoS₂ deposited on SiO₂ pillars in the limit where $2R < a$. b) Raman measurements for highly stressed MoS₂, pinched by SiO₂ pillars. A shift of 8 cm⁻¹ is observed for the E_{12g} between the reference and the peak position at the pillar apex and represents a minimum planar stress of 2%. We assume the difference in intensity is mainly due to the suspended/not-suspended MoS₂. c), Photoluminescence signature of the MoS₂ structure, shown in d) with the signal integrated between 1.3 and 1.6 eV. We observe reduced band gap energy in the strain region, around the pillars. e), some extracted spectrum at the peak apex (red), at a closed position (blue), and at a reference point (purple) (all normalized). At the peak apex, the strong shift of the A and B peaks corresponds to high band gap reduction and a minimum of 2% elongation. We see the appearance of another peak at lower energy, indicated by the black arrow, which we attribute to the indirect band gap in the MoS₂ monolayer under high strain.

Figure 2 shows MoS₂ flakes, which are pinched by a single SiO₂ pillar. This pillar is three times higher than that obtained in similar studies, allowing the strain limits to be reached in such devices. MoS₂ suspended over 2 or three pillars in these tent structures are also presented in Supplementary Information. Using this pillar height, crack propagation in the MoS₂ was observed on the surface. This indicated that the limit of strain in MoS₂ had been reached. In Figure 2b, we present two extreme cases of strain signature at the pillar apex, using Raman spectra. The E_{12g} peak has shifted markedly, by almost 8 cm⁻¹ on the pillars. Using the proportionality $\Delta A_{1g} = 0.26 \cdot \Delta E_{12g}$ (see SI), we calculated a strain of about 2%. Doping and temperature can be excluded, as these cannot be linked to this behavior. This strain estimation is undervalued due to the optical spot size resolution, around 300–400 nm, and the effective broadening of the resulting signal. We assumed that the maximum strain must be reached locally at the nanopillar apex (tens of nanometers). In Figure 2e, the photoluminescence response was measured along a sharp tent structure. Three resonances are visible: A, A and B (around 1.82, 1.85 and 2.0 eV, respectively). A and B correspond to the spin-orbit coupling split of the excitonic resonance and A corresponds to the MoS₂ trion binding energy. Around the pillars, we observed a global resonance shift and large broadening with complex features. This corresponds to a strong band gap reduction of the MoS₂ monolayer, as previously observed.³¹ In our case, the main A peak position, shifted to 1.72 eV. It corresponds to a strain increase of 2.4% around the main structure (see SI). No strong evidence of any Raman peak deviation was observed at the same position. We explain this difference using the so-called phenomenon of exciton funneling.^{23,24} In

contrast to Raman processes, photoluminescence is directly related to optical excitons and can be subjected to diffusive effects which indirectly enhance the emitted signal of the MoS₂ strain. This appears mainly at ambient temperature, where the created excitons diffuse to the pillar apex position, with the minimum band gap value, before emitting a photon at this lower energy. Broadening of the peak indicates it is not fully effective over the length of the spot size and we obviously see different contributions. The optical reflectance is modulated by the MoS₂-substrate cavity (height d_{air}). At less than 0.5 μm around the “tent” structure, d_{air} varies from 600-800 nm to 0 nm and this cavity effect is completely smoothed after convolution with the laser spot. Also, the cavity quality is not enough to enhance the signal dramatically and is not related to the emergence of a strong signal between 1.3 and 1.6 eV in Figure 2.

Closer to the pillar position, an additional contribution appeared at a lower energy and shifted down to about 1.45 eV with an increased shift variation, when compared to the main intensity position. We attribute this peak to the indirect band gap contribution appearing in monolayer MoS₂ with no biaxial strain above 1.5-2%.^{33-43,25} This had been observed previously on the nanoscale³² on a rough substrate with a complex strain tensor and on a smooth substrate, as reference.³¹ In this study, the authors did not notice any additional contributions related to an indirect band gap signature in a suspended MoS₂ monolayer under ultra-large biaxial strain of up to 5.6%. Moreover, the indirect band gap resonance was expected to be less luminescent than a direct process. Compared to the data presented here or ref.,³² our situation was quite different as the nanostructuring gave rise to a strong strain gradient and involved fewer processes, which increased the indirect gap response: 1) The consequences of the exciton funneling effect are not easily determined in this configuration and can favor indirect band gap processes. 2) Suspended MoS₂ has a more intense photoluminescence signal than non-suspended and our suspended part was the stressed region. This improved the indirect peak intensity in our case. 3) Finally, there must be an intermediate regime between uniaxial with random orientation³⁵ and biaxial strain, which results also in divergence from ref.³¹ and affects the modulation of the peak position or intensity *versus* strain.

Discussion

In order to separate, quantify and simulate the 2D properties of a typical Raman pattern, as in Figure 1, it was necessary to understand their contributions to the Raman peak features. For this, different situations were studied where strain, doping, temperature and the number of layers were clearly identified and separated from the other contributions. We focused on the flake of Figure 1c (sample B) with different contributions;

1) The signal position for both the E_{2g}^1 and A_{1g} peaks are shifted by almost 0.4 cm^{-1} . In Figure 3c, a strong linear dependence is seen between the position of the two peaks E_{2g}^1 and A_{1g} with a slope of about 1.1. This indicates a thermal heating effect and should lead to a thermal transport simulation.

2) The observed A_{1g} peak width and peak intensity modulation, which is un-correlated to the E_{2g}^1 peak features, suggested a doping variation. It is reasonable to assume a doping modulation along the sample due to substrate interaction. Doping contributions on the Raman spectrum appear mainly at the A_{1g} peak position.⁴³ We defined n_n as the doping of the MoS₂ layer on the pillars (non-suspended) and n_s elsewhere (suspended). We determined empirically that the main dependence in our results came from the difference $\Delta n = n_s - n_n$.

3) In parallel, some lines are visible between the pillars in the peak position of E_{2g}^1 , which are related to organized ripples and strain; this is less visible in the A_{1g} mapping. Strain at the pillar apex in our sample must not be neglected but can still be avoided if only the monolayer MoS_2 A_{1g} peak dependence is considered. Once the other parameters are well known, the stress at the apex can thus be estimated.

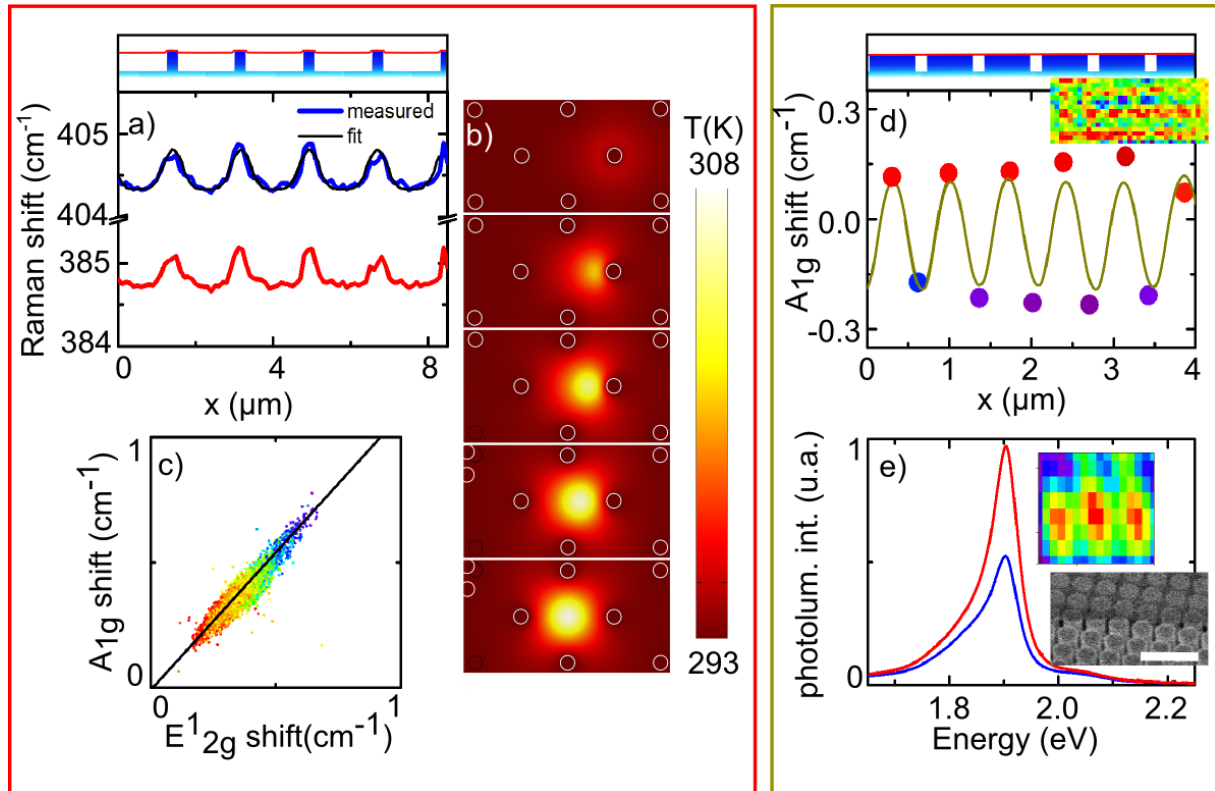


Figure 3: Clean periodic patterns in Raman signatures of the MoS_2 a) Fast Raman mapping of the E_{2g}^1 and A_{2g} peak position shift and intensity along the SiO_2 peak array along the black line in Figure 1c, without any correction. A fit of the A_{2g} peak position is also plotted, taking into account the doping difference of MoS_2 due to substrate interaction and thermal heating, with a thermal conductivity of $50\text{W}\cdot\text{m}^{-1}\cdot\text{K}^{-1}$. c) A Lee diagram,⁴⁵ adapted to MoS_2 , for the points in Figure 1c, with the corresponding color mapping (For clarity small deviations have been removed due to our 15h of measurements). The slope, close to 1, scales well with a temperature dependent signature. The broadening of this plot in the middle part and the curved shape in b indicate, in fact, a more complex schematic with a melting of strain, doping, and temperature. **Doping modulation** with a sample 2R~a. In d), Raman A_{1g} peak modulation along the sample with, in the inset, the corresponding mapping. This modulation indicates a doping change of about $5\cdot 10^{12}\text{ cm}^{-2}$ with a spot size of 300nm. After correlation with the SiO_2 peak intensity we deduced the doping in the suspended part to be higher than in the non-suspended part. e) Photoluminescence spectrum for two positions, on top of a peak (non-suspended) and between the peaks (suspended) with, in the inset, an image of the sample and mapping of the maximum intensity. Scale bar is $1\mu\text{m}$. Only the intensity of the A peak is modulated.

In order to determine the doping variation Δn , we studied a different situation with large $2R \approx a$, where doping was clearly identified and separated from other contributions (Figure 3d). Surfaces with suspended and non-suspended MoS_2 were equivalent and the MoS_2 seemed flat. On the raw data (see SI), a modulation of the A_{1g} peak position can be

observed along the sample, which is less effective in the E_{2g}^1 position. As the signal is quite small, we have to carefully remove the background deviation and average our periodic data to extract the exact ΔE_{2g}^1 and ΔA_{1g} dependence. We obtained $\Delta A_{1g} = 8.2 \Delta E_{2g}^1$, which is definitively a doping dependence signature. In the SI, we proposed a calibration of this value on a non-suspended sample. One limitation of the optical method is the diffraction limit, which has almost the same length as our nanostructures. To avoid this limitation and to be more quantitative, we used an innovative procedure for data analysis. Due to the finite spot size, we took into account that the local doping distribution and the resulting local spectral Raman response were spectrally convoluted with the Gaussian distribution of the laser and the collected photons. The laser diameter was determined with *in-situ* calibration during the same measurement at the MoS₂ flake edge, equivalent to 300 nm. This gave this sample a higher doping score in the suspended part; $\Delta n = +5.10^{12} \text{ cm}^{-1}$. This high doping was also confirmed by the very strong photo-gating observed (see SI) and by the shape of our MoS₂ triangles, which suggested sulfur vacancies.⁴⁴

For the sample in Figure 1c, once the doping on the MoS₂ was known, it was possible to extract the thermal conductivity from the analysis of the A_{1g} position mapping, because the strain effect is negligible on this peak. For the temperature contribution, the local heating, at one point, was obviously induced by the laser itself, and the related Gaussian distribution of the absorbed power. This means that the temperature distribution along the sample was different for every measurement point and it was modeled by finite element analysis with COMSOL software, as in Figure 3b. We naively considered here a thermal transport to be within the Fourier law limit. It is a simple but good approximation for thermal transport in 2D membranes⁴ if we stay in the low heating regime and the typical length scale, between the heat source and the thermal bath, is more or less constant in the measurements presented here. We consider the pillars to be in a perfect thermal contact with the MoS₂, otherwise, no temperature gradient along the MoS₂ would be present nor any effect at all in the Raman data, which was not the case. Our data fit quantitatively and qualitatively well with a spot size of 400 nm and a thermal conductivity of $50 \text{ W} \cdot \text{K}^{-1} \cdot \text{m}^{-1}$, as shown in Figure 3a. The laser spot size is in agreement with previous results. In the SI, we have calibrated the $\Delta A_{1g} / \Delta E_{2g}^1$ ratio for temperature variation on a non-suspended sample. We used a doping difference of $\Delta n = +5.10^{12} \text{ cm}^{-1}$ and a laser power of $50 \mu\text{W}$ and estimated the heating to be at a maximum of around 15 K at when the laser was far away from the pillars. The planar thermal conductivity corresponded to typical values in the literature for suspended monolayer MoS₂ and confirmed our methodology to be appropriate. It must be noted that different Δn were also used to fit our results, with less success. This directly confirms the value of $\Delta n = +5.10^{12} \text{ cm}^{-1}$ to be general in our samples.

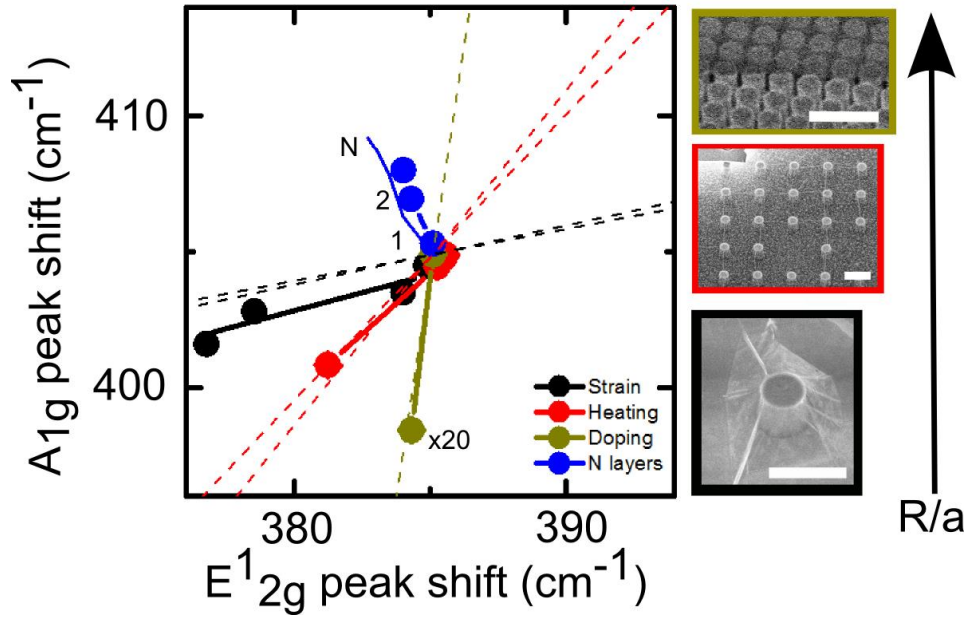


Figure 4: A Lee *et al* diagram⁴⁵ for our different sample configurations for strain, doping temperature and layer number. A plot of the A_{1g} peak positions in function of the E_{2g}^1 peak position is presented for four different cases described in this paper. Blue circles show the number of layer variations compared with the blue reference line (data extracted from).⁴⁹ Black circles show strain variation around the tent structures of Figure 2 compared to the expected slope from the literature (solid black line) and the dashed line for the strain. Red circles show the measurement of heating with the laser itself and brown circles, the doping induced by the pillars.

For this measurement, temperature contributes only about 33% of the total A_{1g} shift position and doping, the rest. With this, the strain at the pillar apex can be calculated from the Raman measurements. For this, we used an analogy between the A_{1g} doping variation and the E_{2g}^1 strain variation. In Figure 4, shown using a Lee *et al.* diagram,⁴⁵ the different cases, with strain, temperature, doping and layer number, with the respective slopes expected from the literature in a dashed line (see SI). Doping and strain variations were extracted from samples and data in Figures 2 and 3, respectively. Temperature variations were obtained for a suspended MoS_2 similar to that in Figure 1c, far away from the SiO_2 pillars, for different laser strengths (10 μW to 500 μW). We can estimate the $\Delta A_{1g} / \Delta E_{2g}^1$ to be around 1.1 as expected in the literature, for thermal heating of a MoS_2 membrane (see SI for references and our own calibration of heating and doping). Three observations can be drawn from these results. First, we confirm that the measurements were done on monolayer MoS_2 for all the data presented, as they have same origins for all the measurements, in accordance with the monolayer MoS_2 case (blue point). Second, the doping, strain, and temperature variations can be optically separated in MoS_2 without any ambiguity. Finally, we have a quasi-mirror symmetry situation between the A_{1g} and the E_{2g}^1 for strain and doping effects, respectively, to the slope of 1. This diagonal corresponds, coincidentally, to the temperature variation.

From this and the slope of about 1 obtained in Figure 3c, it is possible to estimate the strain contribution of about 66% of the peak shift. This mixing of the various contributions with different Raman variations explains, in the Lee *et al.* diagram⁴⁵ of Figure 3c, the broadening of the data in the center region as the strain and doping variations are not completely alike and without the exact same spatial distribution. Nevertheless, it seems that strain and doping contributions are equivalent in a first approximation. In the case of strain, it is necessary, first, to simulate the strain

distribution along the sample with a model that is not trivial in such a suspended configuration.²⁴ Taking advantage of this analogy between strain and doping description, the strain description can be simplified to a simple strain difference $\Delta\varepsilon$ between the suspended ε_s and non-suspended region ε_n , where ε_s and ε_n are assumed to be constant in these regions. With this assumption, there is a real local difference $\Delta\varepsilon$ of around 0.5% between the pillar apex and the suspended area of the sample. It should be noted that in this situation, where strain and doping are symmetric and similar, this configuration can now be used subsequently and extended to more complex features in order to understand more general patterns.

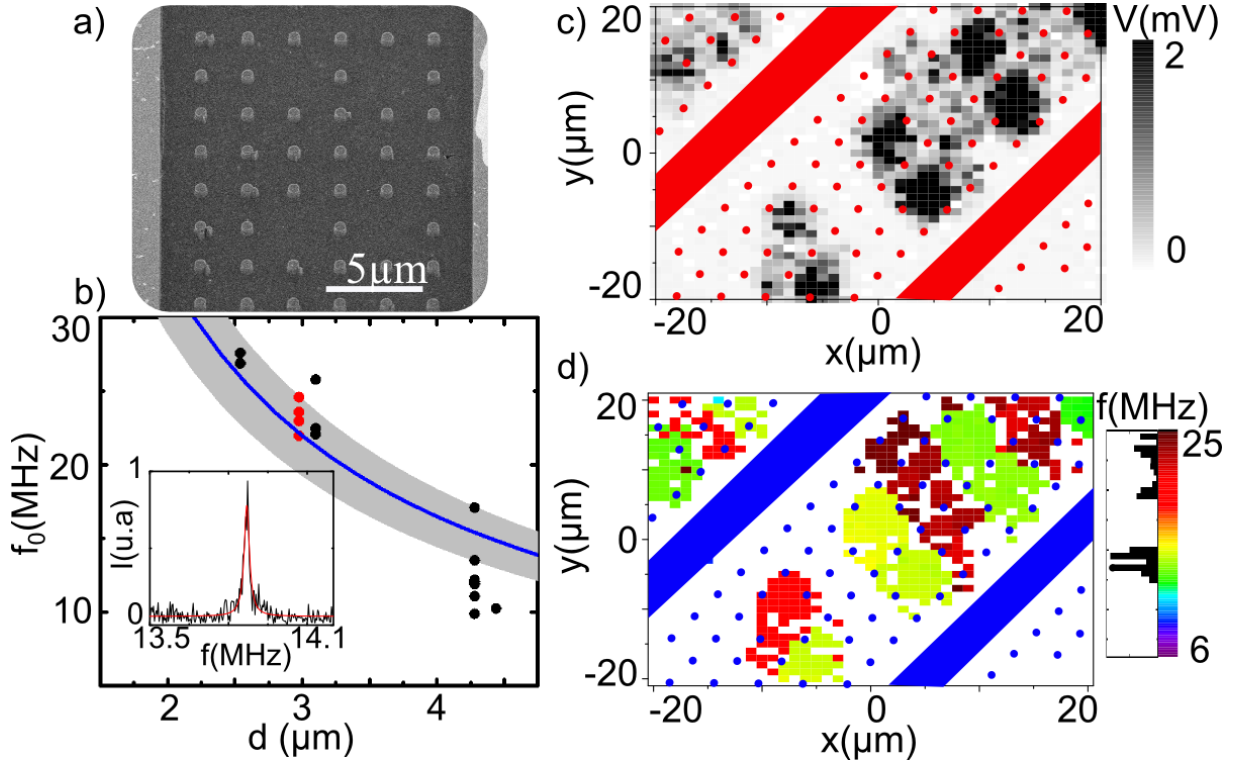


Figure 5: Optomechanical measurement of an array of MoS₂ resonators. a) An E-beam image of suspended MoS₂ over a pillar array with electrical gold contacts S and D on both sides. We used the substrate as a gate G to electrostatically excite the vibration. b) Resonant frequencies as a function of the membrane diameter locally defined by the pillars. Inset shows an example of a resonance with $Q \sim 600$ even at ambient temperature. The blue line corresponds to a strain of $0.045\% \pm 0.01\%$ on the suspended part of the MoS₂. c) and d) spatial mapping of mechanical resonance amplitude and frequency, respectively ($V_G=5V$, $V_{G,ac}=10mV$, $V_{DS}=0V$, He-laser spot size= $4\mu m$, laser power = $12\mu W$).

In Figure 5, we show optomechanical measurements using a quasi-similar set-up, as described in reference.¹⁵ Here, MoS₂ flakes were suspended over pillar arrays, with electrical contacts on each side. This pillar array configuration was previously proposed by Midtvedt *et al.*⁴⁶ in order to create non-linear phononic elements within 2D materials. Each individual membrane was formed locally with 4 pillars or more at the corners. With our samples, we were able to excite electrostatically the vibration with a back gate and to measure it optically with the reflected signal, at 633 nm, a Michelson interferometer and a photodetector. In the inset of Figure 5c, we observe a mechanical resonance of around 13 MHz with a record quality factor ~ 600 for a monolayer MoS₂ vibration at ambient temperature. In Figures 5b and d, we present the amplitude and frequency f_0 of the resonance extracted from a spatial mapping of our resonator array.

Even with our large spot size $\sim 4\mu\text{m}$, we clearly observe a periodic resonator in between the pillar positions. Moreover, the mechanical frequencies are close to each other if we consider similar membrane shapes and dimensions, with low-frequency dispersion. If we analyze the resonances f_0 for different membrane diameters d in different flakes and samples, we find a good match with the Euler Bernoulli description of motion ¹⁷ and with a stress of 0.045% in most of our resonators. This measurement is another factor which highlights the high quality of our devices. A 2D series of resonators has been measured in TMDs and it is proof of the concept that this 2D material can be used for phononic applications only when strain, doping, and heating are well controlled in a periodic device. The mean strain ε_S of 0.045% on the suspended part is a measure for a membrane of dimension d_S ($\sim 3\mu\text{m}$). With the following simple argument, we can deduce the strain on the pillars of diameter d_N ($\sim 280\text{nm}$). If we consider the elongation between the suspended and the non-suspended parts to be more or less equal, we have $\varepsilon_N \sim \varepsilon_S \cdot d_S / d_N = 0.48\%$ which is close to the measured value of 0.5% with Raman. In fact, for a fixed ε_N at the pillar position, we can estimate the membrane strain to diminish when we increase d_S . This is exactly what we observed: for long membranes, the static strain is measured usually below 0.045% and for short membranes, the strain is above this mean value.

Conclusion

In summary, we have achieved nanostructures in monolayer, with monodomain MoS_2 suspended on SiO_2 nanopillars. Using Raman spectroscopy, optomechanical and photoluminescence measurements, we have not only investigated the different contributions from the strain, doping, temperature and layer number but also clearly separated each component. We were able to achieve a clean array of periodically strained MoS_2 and measured an assembly of mechanical resonators in this 2D material. Under these conditions, we have shown the resonator frequency to be homogeneous along the sample for a specific geometry. In order to confirm our protocols and emphasize the doping, strain and temperature effects, we tested samples with $2R \approx a$ and $2R \ll a$ for different laser beam powers. In the limit of $2R \ll a$, where the MoS_2 forms a tent structure, we found a very strong downshift in the optical band gap from 1.89 to 1.45 eV, which originated from the strain. This is partially due to a shift of the direct band gap transition, but also due to the appearance of an indirect band gap. This effect has been optically observed, thanks to the specific geometry and configuration of the devices. For fully suspended $2R < a$ membranes, we were able to extract the doping difference Δn and the thermal properties. From the same measurements, taking advantage of the proportionality between doping and strain effect on Raman peaks, we estimated the strain increase at the pillar apex to be about 0.5%. All these results on MoS_2 nanoengineering can contribute information to the optoelectronic field related to the creation of local quantum emitters with TMDs on pillar arrays, ^{10,11,23} where strain, doping, and temperature are essential parameters. Further studies will explore the mechanics and the possibilities presented by different types of pillar distribution, shedding light on the importance of correlating the geometry of the sample with the strain distribution or the vibration properties. Efficient control of the strain or spring constant with nanostructuring, together with other properties such as doping or temperature, can potentially enhance the properties of force or mass sensitivity within nanomechanical resonators. ^{3,47}

Finally, we report a method to extract the thermal conductivity of our sample. Recent results ⁴⁻⁶ indicate that thermal transport is quite challenging in 2D materials and the record of thermal conductivity ⁷⁻⁹ only represents a part of the phonon mechanism in 2D materials; a major and fundamental aspect is the length dependence of the thermal conductivity in these materials on the nanoscale. Controlling thermal transport or local vibrations by

tailoring the geometry of the system in suspended samples is at the heart of phononics, which today relies mostly on silicon thin film technologies. The extension of this concept to thermal transport in suspended and nanostructured 2D materials will permit the combination of thermal transport engineering with the highest thermal conductive materials.⁸

Acknowledgments: This work was supported by ANR H2DH grants, by the European Union's Horizon 2020 research and innovation program under grant agreement No 732894 (FET Proactive HOT) and by the French Renatech network.

Supporting Information: The Supporting Information is available free of charge on the ACS Publications website. Additional information includes a reference table for MoS₂ Raman peaks and photoluminescence dependence with strain, temperature, and doping, some additional devices of tent structures and large membranes. It details also the procedure for simulations, an additional calibration for the temperature effect, some doping effect on Raman measurements. We have included the mechanical model for our 2D drums

Conflicting financial interests: The authors declare no conflicting financial interests.

REFERENCES

- (1) Chaste, J.; Saadani, A.; Jaffre, A.; Madouri, A.; Alvarez, J.; Pierucci, D.; Ben Aziza, Z.; Ouerghi, A. Nanostructures in Suspended Mono- and Bilayer Epitaxial Graphene. *Carbon* **2017**, *125*, 162–167.
- (2) Blees, M. K.; Barnard, A. W.; Rose, P. A.; Roberts, S. P.; McGill, K. L.; Huang, P. Y.; Ruyack, A. R.; Kevek, J. W.; Kobrin, B.; Muller, D. A.; McEuen, P. L. Graphene Kirigami. *Nature* **2015**, *524*, 204–207.
- (3) Kumar, M.; Bhaskaran, H. Ultrasensitive Room-Temperature Piezoresistive Transduction in Graphene-Based Nanoelectromechanical Systems. *Nano Lett.* **2015**, *15*, 2562–2567.
- (4) Cepellotti, A.; Fugallo, G.; Paulatto, L.; Lazzeri, M.; Mauri, F.; Marzari, N. Phonon Hydrodynamics in Two-Dimensional Materials. *Nat. Commun.* **2015**, *6*.
- (5) Fugallo, G.; Cepellotti, A.; Paulatto, L.; Lazzeri, M.; Marzari, N.; Mauri, F. Thermal Conductivity of Graphene and Graphite: Collective Excitations and Mean Free Paths. *Nano Lett.* **2014**, *14*, 6109–6114.
- (6) Xu, X.; Pereira, L. F. C.; Wang, Y.; Wu, J.; Zhang, K.; Zhao, X.; Bae, S.; Bui, C. T.; Xie, R.; Thong, J. T. L.; Hong, B. H.; Loh, K. P.; Donadio, D.; Li, B.; Özyilmaz, B. Length-Dependent Thermal Conductivity in Suspended Single-Layer Graphene. *Nat. Commun.* **2014**, *5*, 3689.
- (7) Ghosh, S.; Bao, W.; Nika, D. L.; Subrina, S.; Pokatilov, E. P.; Lau, C. N.; Balandin, A. A. Dimensional Crossover of Thermal Transport in Few-Layer Graphene. *Nat. Mater.* **2010**, *9*, 555–558.
- (8) Balandin, A. A.; Ghosh, S.; Bao, W.; Calizo, I.; Teweldebrhan, D.; Miao, F.; Lau, C. N. Superior Thermal Conductivity of Single-Layer Graphene. *Nano Lett.* **2008**, *8*, 902–907.
- (9) Balandin, A. A. Phonon Engineering in Graphene and van Der Waals Materials. *MRS Bull.* **2014**, *39*, 817–823.
- (10) Branny, A.; Kumar, S.; Proux, R.; Gerardot, B. D. Deterministic Strain-Induced Arrays of Quantum Emitters in a Two-Dimensional Semiconductor. *Nat. Commun.* **2017**, *8*, 15053.

- (11) Palacios-Berraquero, C.; Kara, D. M.; Montblanch, A. R.-P.; Barbone, M.; Latawiec, P.; Yoon, D.; Ott, A. K.; Loncar, M.; Ferrari, A. C.; Atatüre, M. Large-Scale Quantum-Emitter Arrays in Atomically Thin Semiconductors. *Nat. Commun.* **2017**, *8*, 15093.
- (12) Kumar, S.; Kaczmarczyk, A.; Gerardot, B. D. Strain-Induced Spatial and Spectral Isolation of Quantum Emitters in Mono- and Bi-Layer {WSe}₂. *Nano Lett.* **2015**, *15*, 7567–7573.
- (13) Kern, J.; Niehues, I.; Tonndorf, P.; Schmidt, R.; Wigger, D.; Schneider, R.; Stiehm, T.; Michaelis de Vasconcellos, S.; Reiter, D. E.; Kuhn, T.; Bratschitsch, R. Nanoscale Positioning of Single-Photon Emitters in Atomically Thin WSe₂. *Adv. Mater.* **2016**, *28*, 7101–7105.
- (14) Shepard, G. D.; Ajayi, O. A.; Li, X.; Zhu, X.-Y.; Hone, J.; Strauf, S. Nanobubble Induced Formation of Quantum Emitters in Monolayer Semiconductors. *2D Mater* **2017**, *4*, 21019.
- (15) Morell, N.; Reserbat-Plantey, A.; Tsioutsios, I.; Schädler, K. G.; Dubin, F.; Koppens, F. H. L.; Bachtold, A. High Quality Factor Mechanical Resonators Based on WSe₂ Monolayers. *Nano Lett.* **2016**, *16*, 5102–5108.
- (16) Liu, C.-H.; Kim, I. S.; Lauhon, L. J. Optical Control of Mechanical Mode-Coupling within a MoS₂ Resonator in the Strong-Coupling Regime. *Nano Lett.* **2015**, *15*, 6727–6731.
- (17) Lee, J.; Wang, Z.; He, K.; Shan, J.; Feng, P. X.-L. High Frequency MoS₂ Nanomechanical Resonators. *ACS Nano* **2013**, *7*, 6086–6091.
- (18) Reserbat-Plantey, A.; Schädler, K. G.; Gaudreau, L.; Navickaite, G.; Güttinger, J.; Chang, D.; Toninelli, C.; Bachtold, A.; Koppens, F. H. L. Electromechanical Control of Nitrogen-Vacancy Defect Emission Using Graphene {NEMS}. *Nat. Commun.* **2016**, *7*, 10218.
- (19) Yeo, I.; Assis, P.-L. de; Gloppe, A.; Dupont-Ferrier, E.; Verlot, P.; Malik, N. S.; Dupuy, E.; Claudon, J.; Gérard, J.-M.; Auffèves, A.; Nogues, G.; Seidelin, S.; Poizat, J-Ph.; Arcizet, O.; Richard, M. Strain-Mediated Coupling in a Quantum Dot–mechanical Oscillator Hybrid System. *Nat. Nanotechnol.* **2014**, *9*, 106.
- (20) Wang, Z.; Lee, J.; He, K.; Shan, J.; Feng, P. X.-L. Embracing Structural Nonidealities and Asymmetries in Two-Dimensional Nanomechanical Resonators. *Sci. Rep.* **2014**, *4*.
- (21) Castellanos-Gomez, A.; Singh, V.; van der Zant, H. S. J.; Steele, G. A. Mechanics of Freely-Suspended Ultrathin Layered Materials. *Ann. Phys.* **2015**, *527*, 27–44.
- (22) Leeuwen, R. van; Castellanos-Gomez, A.; Steele, G. A.; Zant, H. S. J. van der; Venstra, W. J. Time-Domain Response of Atomically Thin MoS₂ Nanomechanical Resonators. *Appl. Phys. Lett.* **2014**, *105*, 041911.
- (23) Li, H.; Contryman, A. W.; Qian, X.; Ardakani, S. M.; Gong, Y.; Wang, X.; Weisse, J. M.; Lee, C. H.; Zhao, J.; Ajayan, P. M.; Li, J.; Manoharan H.C.; Zheng, X. Optoelectronic Crystal of Artificial Atoms in Strain-Textured Molybdenum Disulphide. *Nat. Commun.* **2015**, *6*, 7381.
- (24) Feng, J.; Qian, X.; Huang, C.-W.; Li, J. Strain-Engineered Artificial Atom as a Broad-Spectrum Solar Energy Funnel. *Nat. Photonics* **2012**, *6*, 866–872.
- (25) Furchi, M. M.; Polyushkin, D. K.; Pospischil, A.; Mueller, T. Mechanisms of Photoconductivity in Atomically Thin MoS₂. *Nano Lett.* **2014**, *14*, 6165–6170.
- (26) Reserbat-Plantey, A.; Kalita, D.; Han, Z.; Ferlazzo, L.; Autier-Laurent, S.; Komatsu, K.; Li, C.; Weil, R.; Ralko, A.; Marty, L.; Guéron, S.; Bendiab, N.; Bouchiat, H.; Bouchiat, V. Strain Superlattices and Macroscale Suspension of Graphene Induced by Corrugated Substrates. *Nano Lett.* **2014**, *14*, 5044–5051.
- (27) Wang, Z.; Feng, P. X.-L. Interferometric Motion Detection in Atomic Layer 2D Nanostructures: Visualizing Signal Transduction Efficiency and Optimization Pathways. *Sci. Rep.* **2016**, *6*, 28923.

- (28) Henck, H.; Pierucci, D.; Chaste, J.; Naylor, C. H.; Avila, J.; Balan, A.; Silly, M. G.; Asensio, M. C.; Sirotti, F.; Johnson, A. T. C.; Lhuillier, E.; Ouerghi, A. Electrolytic Phototransistor Based on Graphene-MoS₂ van Der Waals p-n Heterojunction with Tunable Photoresponse. *Appl. Phys. Lett.* **2016**, *109*, 113103.
- (29) Pierucci, D.; Henck, H.; Avila, J.; Balan, A.; Naylor, C. H.; Patriarcho, G.; Dappe, Y. J.; Silly, M. G.; Sirotti, F.; Johnson, A. T. C.; Asensio, M. C.; Ouerghi, A. Band Alignment and Minigaps in Monolayer MoS₂-Graphene van Der Waals Heterostructures. *Nano Lett.* **2016**, *16*, 4054–4061.
- (30) Jin, C. Large Deflection of Circular Membrane under Concentrated Force. *Appl Math Mech-Engl Ed* **2008**, *29*, 889–896.
- (31) Lloyd, D.; Liu, X.; Christopher, J. W.; Cantley, L.; Wadehra, A.; Kim, B. L.; Goldberg, B. B.; Swan, A. K.; Bunch, J. S. Band Gap Engineering with Ultralarge Biaxial Strains in Suspended Monolayer MoS₂. *Nano Lett.* **2016**, *16*, 5836–5841.
- (32) Shin, B. G.; Han, G. H.; Yun, S. J.; Oh, H. M.; Bae, J. J.; Song, Y. J.; Park, C.-Y.; Lee, Y. H. Indirect Bandgap Puddles in Monolayer MoS₂ by Substrate-Induced Local Strain. *Adv. Mater.* **2016**, *28*, 9378–9384.
- (33) Steinhoff, A.; Kim, J.-H.; Jahnke, F.; Rösner, M.; Kim, D.-S.; Lee, C.; Han, G. H.; Jeong, M. S.; Wehling, T. O.; Gies, C. Efficient Excitonic Photoluminescence in Direct and Indirect Band Gap Monolayer MoS₂. *Nano Lett.* **2015**, *15*, 6841–6847.
- (34) Lu, P.; Wu, X.; Guo, W.; Zeng, X. C. Strain-Dependent Electronic and Magnetic Properties of MoS₂ Monolayer, Bilayer, Nanoribbons and Nanotubes. *Phys Chem Chem Phys* **2012**, *14*, 13035–13040.
- (35) Conley, H. J.; Wang, B.; Ziegler, J. I.; Haglund, R. F.; Pantelides, S. T.; Bolotin, K. I. Bandgap Engineering of Strained Monolayer and Bilayer MoS₂. *Nano Lett.* **2013**, *13*, 3626–3630.
- (36) Scheuschner, N.; Ochedowski, O.; Kaulitz, A.-M.; Gillen, R.; Schleberger, M.; Maultzsch, J. Photoluminescence of Freestanding Single- and Few-Layer MoS₂. *Phys. Rev. B* **2014**, *89*, 125406.
- (37) Rice, C.; Young, R. J.; Zan, R.; Bangert, U.; Wolverson, D.; Georgiou, T.; Jalil, R.; Novoselov, K. S. Raman-Scattering Measurements and First-Principles Calculations of Strain-Induced Phonon Shifts in Monolayer MoS₂. *Phys. Rev. B* **2013**, *87*, 81307.
- (38) Zhu, C. R. Strain Tuning of Optical Emission Energy and Polarization in Monolayer and Bilayer MoS₂. *Phys. Rev. B* **2013**, *88*.
- (39) Castellanos-Gomez, A.; Roldán, R.; Cappelluti, E.; Buscema, M.; Guinea, F.; van der Zant, H. S. J.; Steele, G. A. Local Strain Engineering in Atomically Thin MoS₂. *Nano Lett.* **2013**, *13*, 5361–5366.
- (40) He, K.; Poole, C.; Mak, K. F.; Shan, J. Experimental Demonstration of Continuous Electronic Structure Tuning *via* Strain in Atomically Thin MoS₂. *Nano Lett.* **2013**, *13*, 2931–2936.
- (41) Hui, Y. Y.; Liu, X.; Jie, W.; Chan, N. Y.; Hao, J.; Hsu, Y.-T.; Li, L.-J.; Guo, W.; Lau, S. P. Exceptional Tunability of Band Energy in a Compressively Strained Trilayer MoS₂ Sheet. *ACS Nano* **2013**, *7*, 7126–7131.
- (42) Roldán, R.; Castellanos-Gomez, A.; Cappelluti, E.; Guinea, F. Strain Engineering in Semiconducting Two-Dimensional Crystals. *J Phys Condens Matter* **2015**, *27*, 313201.
- (43) Chakraborty, B.; Bera, A.; Muthu, D. V. S.; Bhowmick, S.; Waghmare, U. V.; Sood, A. K. Symmetry-Dependent Phonon Renormalization in Monolayer MoS₂ Transistor. *Phys. Rev. B* **2012**, *85*, 161403.
- (44) Kim, I. S.; Sangwan, V. K.; Jariwala, D.; Wood, J. D.; Park, S.; Chen, K.-S.; Shi, F.; Ruiz-Zepeda, F.; Ponce, A.; Jose-Yacaman, M.; Dravid, V. P.; Marks, T. J.; Hersam, M. C.; Lauhon, L. J. Influence of Stoichiometry on the Optical and Electrical Properties of Chemical Vapor Deposition Derived MoS₂. *ACS Nano*

2014, 8, 10551–10558.

(45) Lee, J. E.; Ahn, G.; Shim, J.; Lee, Y. S.; Ryu, S. Optical Separation of Mechanical Strain from Charge Doping in Graphene. *Nat. Commun.* **2012**, 3, 1024.

(46) Midtvedt, D.; Isacsson, A.; Croy, A. Nonlinear Phononics Using Atomically Thin Membranes. *Nat. Commun.* **2014**, 5, 4838.

(47) Chaste, J.; Eichler, A.; Moser, J.; Ceballos, G.; Rurali, R.; Bachtold, A. A Nanomechanical Mass Sensor with Yoctogram Resolution. *Nat. Nanotechnol.* **2012**, 7, 301–304.

(48) Lee, C.; Yan, H.; Brus, L. E.; Heinz, T. F.; Hone, J.; Ryu, S. Anomalous Lattice Vibrations of Single- and Few-Layer MoS₂. *ACS Nano* **2010**, 4, 2695–2700.

Supplementary information for:

Intrinsic properties of suspended MoS₂ on SiO₂/Si pillar arrays for nanomechanics and optics.

Julien Chaste^{1*}, Amine Missaoui¹, Si Huang¹, Hugo Henck¹, Zeineb Ben Aziza¹, Laurence Ferlazzo¹, Adrian Balan², Alan. T. Charlie Johnson Jr.², Rémy Braive^{1,3}, Abdelkarim Ouerghi¹

¹ Centre de Nanosciences et de Nanotechnologies, CNRS, Univ. Paris-Sud, Université Paris-Saclay, C2N – Marcoussis

²Department of Physics and Astronomy, University of Pennsylvania, 209S 33rd Street, Philadelphia, Pennsylvania 19104 6396, United States

³Université Paris Diderot, Sorbonne Paris Cité, 75207 Paris Cedex 13, France

* Corresponding author: julien.chaste@c2n.upsaclay.fr

S1: Examples of nanostructuring with nanopillars

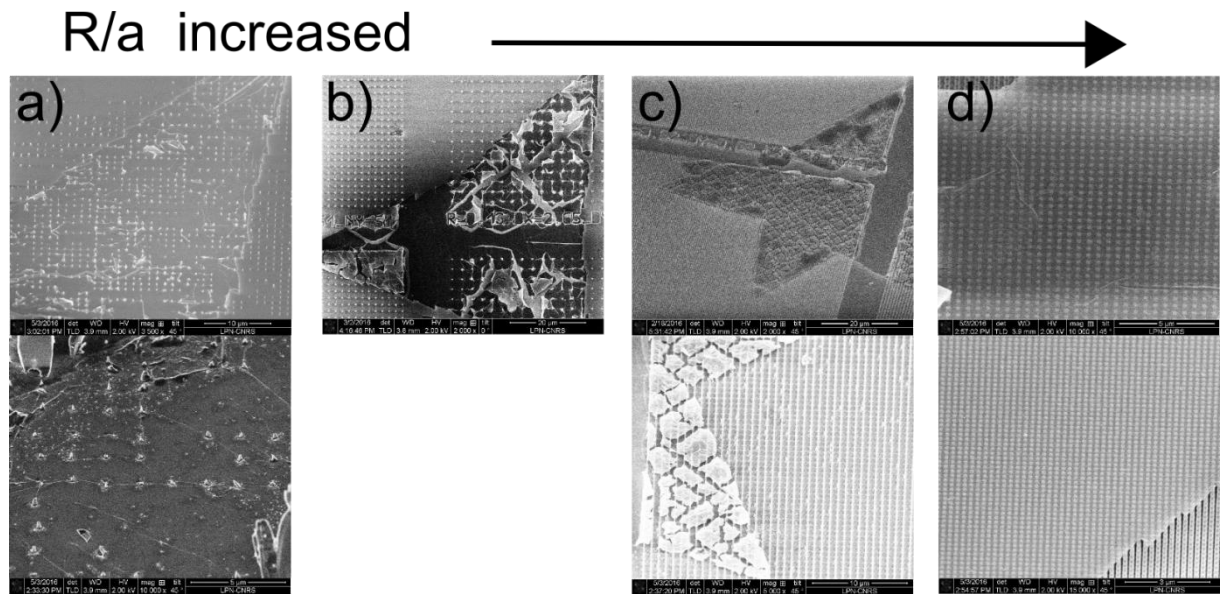


Figure S1a: Electron beam images of MoS₂ on nanopillar arrays with different Radii, R and period a. From a) to d) the R/a ratio increases and, consequently, the mechanical stability of the suspended structure against cracking and ripples. In a) we can see the same type of ripple organization as in the reference ¹. The shape and structure of membrane cracks and ripples are correlated with the pillar structure.

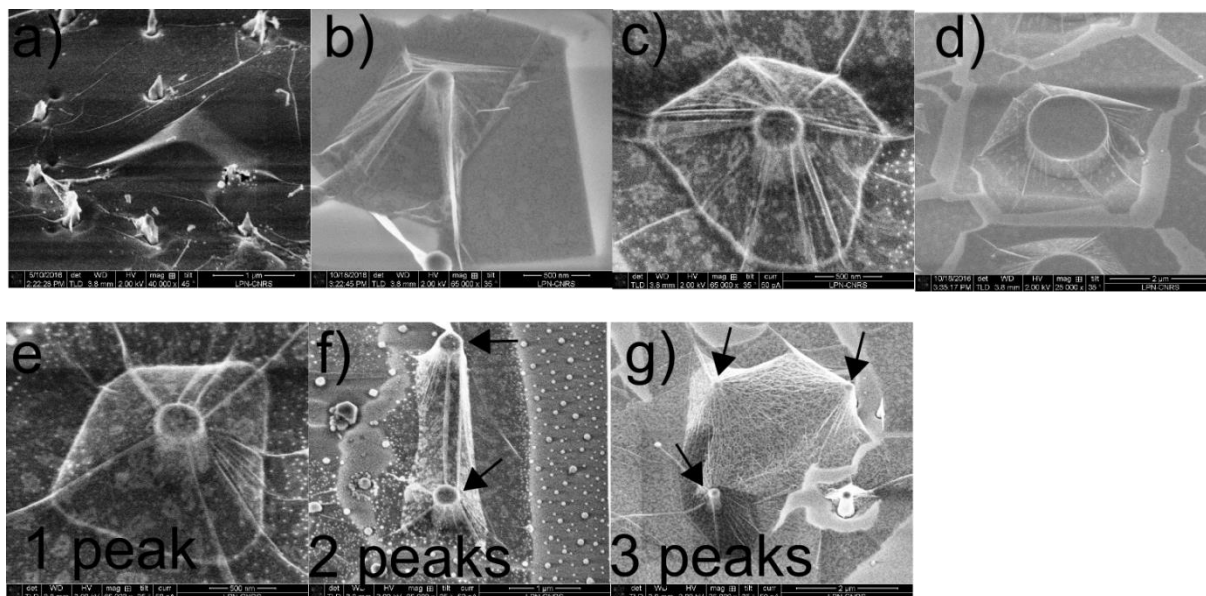


Figure S1b: Tent structures with tall pillar height. In the regime defined in Figure S1a-a, we see a large amount of “tent” formed by MoS₂ covering pillars with different pillar radii and heights. In a) to d), the radius increases. It is possible to build tent structures with heights of 600-820nm in comparison with ref¹⁻³ the height does not go above 200 nm. In e) to g), we see different tent structures with two or three pillars.

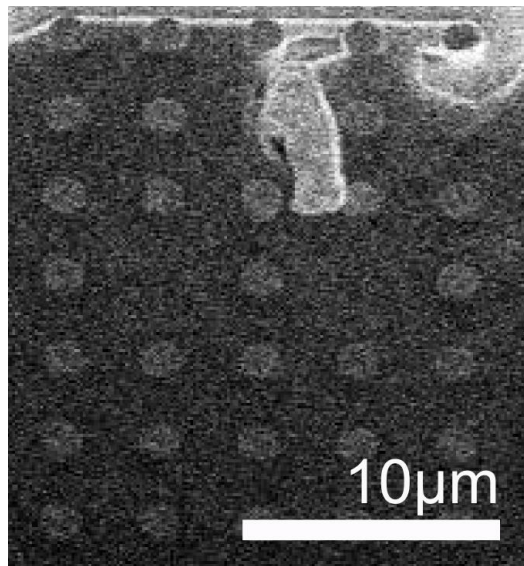


Figure S1c: Very large suspended structures. When the transfer process is optimized, our method creates arrays of MoS₂ square membranes with 6.5 μ m sides.

S2: MoS2, Raman, and photoluminescence

The table shows citations for the Raman peaks E_{2g} and A_{1g} and the photoluminescence peaks A, B, and I) as a function of doping, strain, and temperature for different layer numbers. The peak shift depends on the substrate interaction, the nature of stress applied to the sample, the number of layers or the temperature.

Raman peak and photoluminescence peak behavior in relation to strain, doping and temperature

N-layer	Peaks	Strain (cm-1/%) strain (meV/%)	Doping (/10 ¹³ cm ⁻²)	Temperature cm ⁻¹ /100K
1	E_{2g}	-5.2(bi,sus) ⁴ , -4.6(bi) ⁵ , -2.1 (uni) ⁶ , -4.5/-1(uni) ⁷ , -1.3(uni) ⁸ , -2.5/-0.8 ⁹	-0.33 ¹⁰	-1.3 ¹¹ ,
	A_{1g}	-1.7(bi,sus) ⁴ , -1(bi) ⁵ , -0.4(uni) ⁶ , -0.4(uni) ⁸	-2.2 ¹⁰	-1.6 ¹¹
	A	-99(bi,sus) ⁴ , 95(bi) ⁵ , -45(uni) ⁷ , 44(th) ¹² , -25 ⁸ , -64 ¹³ , -48 ¹⁴	-70(th) ^{15*} , -66 ^{16*}	
2	E_{2g}	-5.2(th,bi,sus) ¹⁷ , -4.6/-1(uni) ⁷⁺		
	A_{1g}	-2.2(th,bi,sus) ¹⁷		
	A	-120(th,bi,sus) ¹⁷ , -91(bi,sus) ⁴ , -53(uni) ⁷ , -48 ¹³ , -46 ¹⁴		
	I	-290(th,bi,sus) ¹⁷ , -144(bi,sus) ⁴ , -120(uni) ⁷ , -77 ¹³ , -86 ¹⁴		
N	E_{2g}	1.7(uni,sus) ¹⁸ , -1.7(uni) ⁶ , -3.7(uni) ⁸		-1.5 ¹¹ , -1.32 ¹⁹
	A_{1g}	-0.4(uni) ⁶ , -0.7(uni) ⁸		-1.3 ¹¹ , -1.23 ¹⁹
	A	-73(bi,sus) ⁴ , -60 ⁸		
	I	-110(bi,sus) ⁴		

*=indirect deduction from graph and text, += E+ et E- measurements after splitting,

Sus=suspended, Bi=biaxial, uni=uniaxial

S3: MoS2 on pillars: in relation to doping

In our samples, part of the MoS₂ was suspended and part was on the SiO₂ surface, at the SiO₂ pillar apex, for example. The first well-known characteristic of a system such as a 2D material is the strong doping dependence and interaction with the substrate, especially in the case of MoS₂.²⁰ If the material was suspended with a doping n_s or on a SiO₂ substrate with a doping n_n , the Fermi level was seen to shift up to 40meV.¹⁷

The case of doping is easier to simulate than strain and heating because this depends only on n_n , n_s and D : the doping in the non-suspended and suspended parts and the laser spot size, respectively. In addition, both n_n and n_s must be quite similar from one sample to the other. In order to define n_s and n_n , it is possible to measure a reference to a large suspended sample and a large non-suspended part, as in ref¹⁷ for bilayer MoS₂. In our case, we needed a calibration *in situ* due to the small deviations in the reference peak position because of doping ($\leq 1\text{cm}^{-1}$). Our problem was that the doping effect was reduced to an effective doping because the pillar dimensions were smaller than the spot dimensions. The effective doping had an intermediate value between n_n and n_s . The effect of doping on Raman peak concerned mainly the A_{1g} peak.

In periodic patterns such as in Figure 3, with $R=0.215\mu\text{m}$ and $a=0.5\mu\text{m}$, we could measure modulation of the A_{1g} peak position. We extracted the effective peak intensity modulation, defined as the ratio $I_{\text{max}}/I_{\text{min}}$ and dP , which is the effective difference in peak position at maximum and minimum intensities. This modulation came from doping, as presented by the Lee *et al* diagram²¹ for the two peak positions (Figure S3c). The photoluminescence intensity of the A peak also shows a strong modulation without energy shift of the peaks or intensity variation of the A- and B peaks (Figure 3), being a signature of the doping variation in the MoS₂ along the structure.

For doping simulations, we assumed an initial Lorentzian peak for the suspended MoS₂ with a typical width $W_s=5.5\text{cm}^{-1}$, and position $P_s=405\text{cm}^{-1}$ for the A_{1g} peak (height H_s set to 1 by default for the undoped suspended situation). We fixed the Raman peak dependence as a function of ref¹⁰, taking $df=4.(n_n-n_s)/1.8$, for $H=1+n_n/s/1.8$, $W=5.5+n_n.s.(12-5.5)$ (df in cm^{-1} , n_n in 10^{13}cm^{-2} H in u.a., and W in cm^{-1}). The Gaussian spot size was around 300-400nm in most of our data but remaining a free parameter in our simulations. We calibrated this at the edge of the MoS₂ (Figure S3b). With the measurement of $I_{\text{max}}/I_{\text{min}}$ and df , it was possible to define D , n_n and n_n . In the case of Figure 3, we found, after convolution of local mapping for the measured photon intensity with the Gaussian spot size, $I_{\text{max}}/I_{\text{min}}=1.25$ and $dP=0.28\text{cm}^{-1}$. This gave a real peak position difference df of 1.1cm^{-1} ,

a doping difference $\Delta n = n_s - n_n = 5.10^{12} \text{cm}^{-1}$, a real width $W_n = 7.3 \text{cm}^{-1}$, an intensity $H_n = 1.72$ and a Gaussian spot size of $D = 300 \text{nm}$.

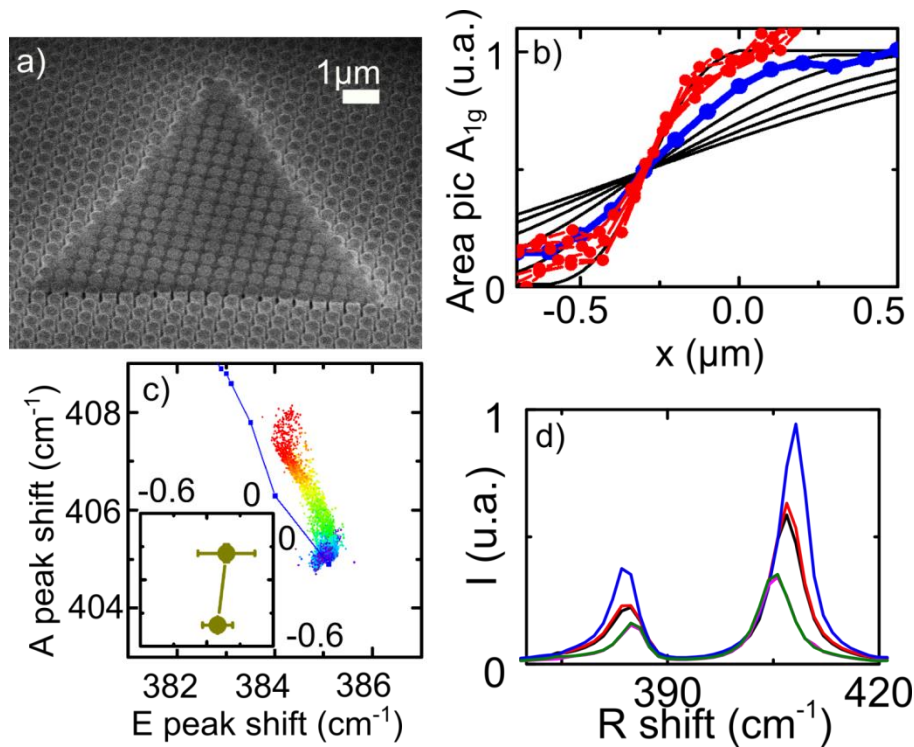


Figure S3a: MoS₂ flake on top of pillars with 2R~a: layer number variation and Gaussian spot size calibration a) e-beam image of a MoS₂ flake with different layer numbers. b) The Gaussian spot size calibration with A_{1g} peak intensity in blue and red taken at the red and blue bar positions in Figure S3b. In black, the fit of Lorentzian area, along with a step in intensity, correlated with a 2D Gaussian spot size, normalized at 1 (Diameters of 200, 400, 600, 800, 1000, 1200nm). The spot size is between 300 and 400nm. c) Diagram of the respective peak positions of MoS₂ for the whole points present in Raman mapping. This corresponds closely to the variation in the number of layers (blue line). In the inset, we drew the same diagram along the peaks for suspended and non-suspended parts in Figure 3d after background removal and averaging. A doping variation was identified. In d, the different spectra for 1 layer, 2 layers, and N layers.

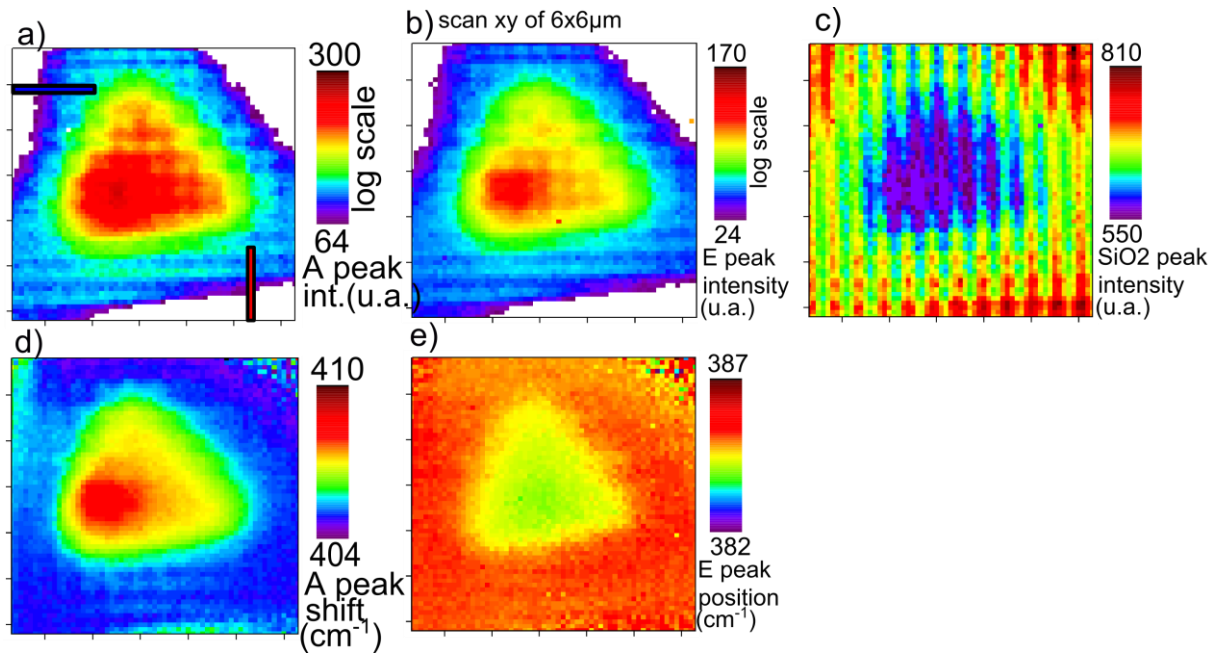


Figure S3b: MoS2 flake on top of pillars with 2R~a: additional data for Figure S3b. Raman mapping of A_{1g} and E_{2g}^1 data for intensity (a, b) and peak shift (d, e) In (d) and (e) we have raw data on the left and background subtracted data on the right. In (c), the SiO_2 peak intensity defines the peak position. A modulation of the shift with pillars is only observed for the A_{1g} peak; this indicates a doping modulation.

General relationship between material properties and Raman peak shape when a nanostructure and a high gradient are present

In order to determine properly the real local peak position and intensity in the suspended and non-suspended parts from the convoluted measured data, we used the following two methods: a simple and intuitive method with a strong approximation and an exact methodology. The approximated method is empirically valid for small or gentle variations, i.e. when the peak shift is less than 1cm^{-1} and can diverge for greater variations.

First, we define an xy map for the different property variations. The easier method is simply to convolute this mapping with a 2D Gaussian distribution at each point and to transform it into frequency shift or peak intensity. To be exact, we measured all the collected Raman photons, with a Gaussian distribution around the spot center. This meant we had to convolute the Raman intensity at each Raman frequency (cm^{-1}) after the peak intensity at each point had become modified by the local strain, doping or temperature. This is much more precise and general, but it is not intuitive,

because the peak can have a non-standard shape if the gradient shift is too high and the peak variation mapping is not necessarily linear with the doping, strain or temperature mapping.

For the sample in Figure 1c, $R=0.13\mu\text{m}$, and $a=1.21\mu\text{m}$. We estimated, in a first step, the doping to be $\Delta n=n_s-n_n=5.10^{12}\text{cm}^{-1}$. On a second step, we tested different doping differences Δn and found a result which can converge only for doping values around $=5.10^{12}\text{cm}^{-1}$ (see Figure S4d). This confirms the previous calibration.

The value of $\Delta n=n_s-n_n=5.10^{12}\text{cm}^{-1}$ was quite unexpected because the suspended part of the MoS_2 is usually less doped due to less interaction with the substrate and without an external doping source. Our result means our MoS_2 is naturally doped and the doping is reduced by the SiO_2 interaction. To explain this, we have to consider the specific case of our MoS_2 . In Figure S3d, we can see MoS_2 flakes that are not really triangular. This is a result of sulfur vacancy in the MoS_2 , as described in ref.²² We have previously measured the natural doping of the MoS_2 appearing in our devices,^{23,24} which is not negligible. In addition to this, we carried out electrical measurements on a suspended MoS_2 flake between 2 electrical contacts. As shown in Figure S3d, there is strong photogating appearing in the suspended MoS_2 , even with a low power laser. The efficiency of this photogating, compared to non-suspended devices with the same MoS_2 ²⁴ is the proof that our devices can be more doped in the suspended than in the undoped parts, with the laser illumination lower than in Raman spectroscopy, where the laser power is usually around $50\mu\text{W}$.

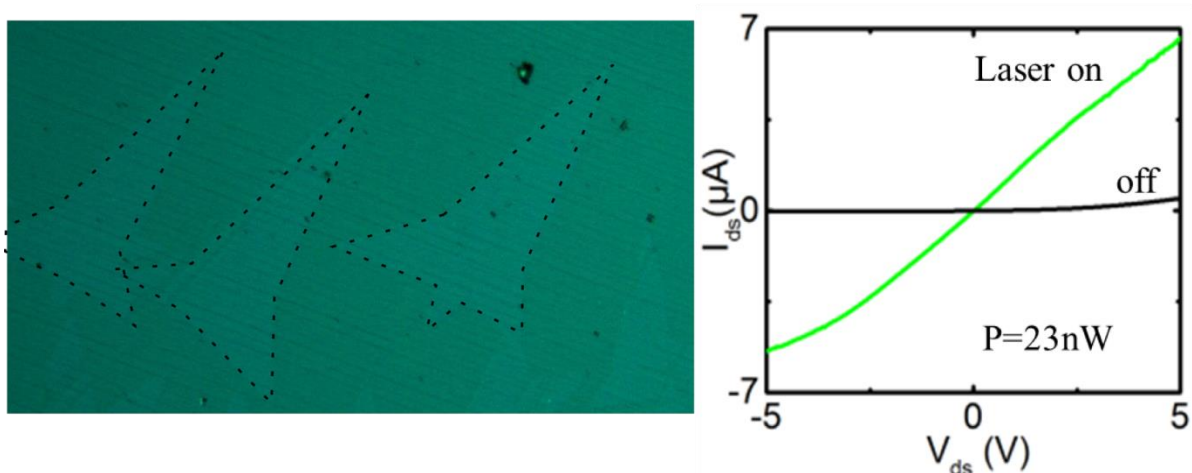


Figure S3d: typical MoS_2 with sulfur vacancies and doping in suspended samples. An optical image of typical MoS_2 flakes with convex edges. This is a signature of sulfur vacancies in our MoS_2 and can explain a natural doping by dopants localized in MoS_2 at the sulfur

vacancies. An I(V) curve of a typical suspended MoS₂ flake with and without illumination at 532nm. We observed a dark state in the OFF position and an Ohmic conductance in the ON position, even with only 23nW. This means we activated strong photogating in our devices, which can explain the doping difference $\Delta n = 5 \cdot 10^{12} \text{cm}^{-2}$ appearing in our Raman measurements.

S4: MoS₂ on pillars: in relation to heating

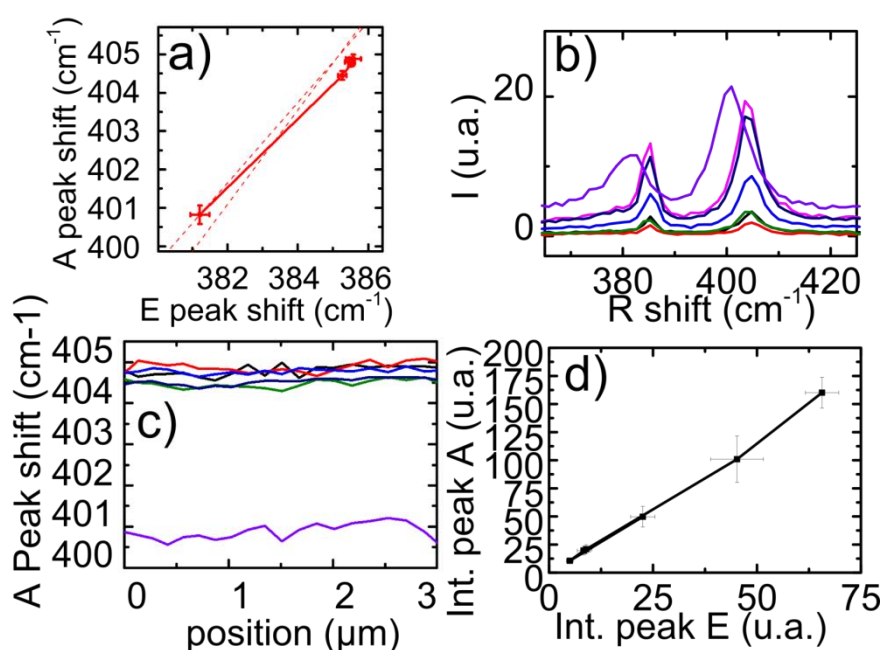


Figure S4a: Laser heating effect on suspended monolayer MoS₂. b) Raman spectral measurements on a MoS₂ flake suspended between pillars in the limit $2R < a$, and with a geometry very similar to the sample in Figure 1c ($P=5, 10, 50, 100, 500 \mu\text{W}$). The data was

taken at the center of the suspended area, far away from the pillars. c) The A_{1g} Peak position along the suspended MoS_2 as a function of laser power. This is quite homogenous. a) A Lee et al. diagram of the respective peak positions for the average points in c and for every laser power intensity. d) The same diagram with the peak intensity. Both confirm a shift due to heat in the sample, with a slope close to 1.1 for the position.

In order to determine the heating effect on our samples, especially the ratio $\Delta A_{1g} / \Delta E_{2g}^1$ we used a very simple methodology. We used a sample of suspended monolayer MoS_2 on SiO_2 pillars similar to the sample in Figure 1b. We placed the laser between pillars and we measured the Raman signal as a function of the laser power, especially the peak position and the ratio $\Delta A_{1g} / \Delta E_{2g}^1$. We repeated the same measurement along a suspended membrane (each point being away from the pillars) to determine the small standard deviation of our measurement. We did observe a broadening of the Raman peak at high powers and a linear variation between the two Raman peak intensities, as expected from the heating variation of the MoS_2 membrane. This method involves some approximations, but the result is completely in accordance with the literature and a $\Delta A_{1g} / \Delta E_{2g}^1$ ratio of around 1.1.

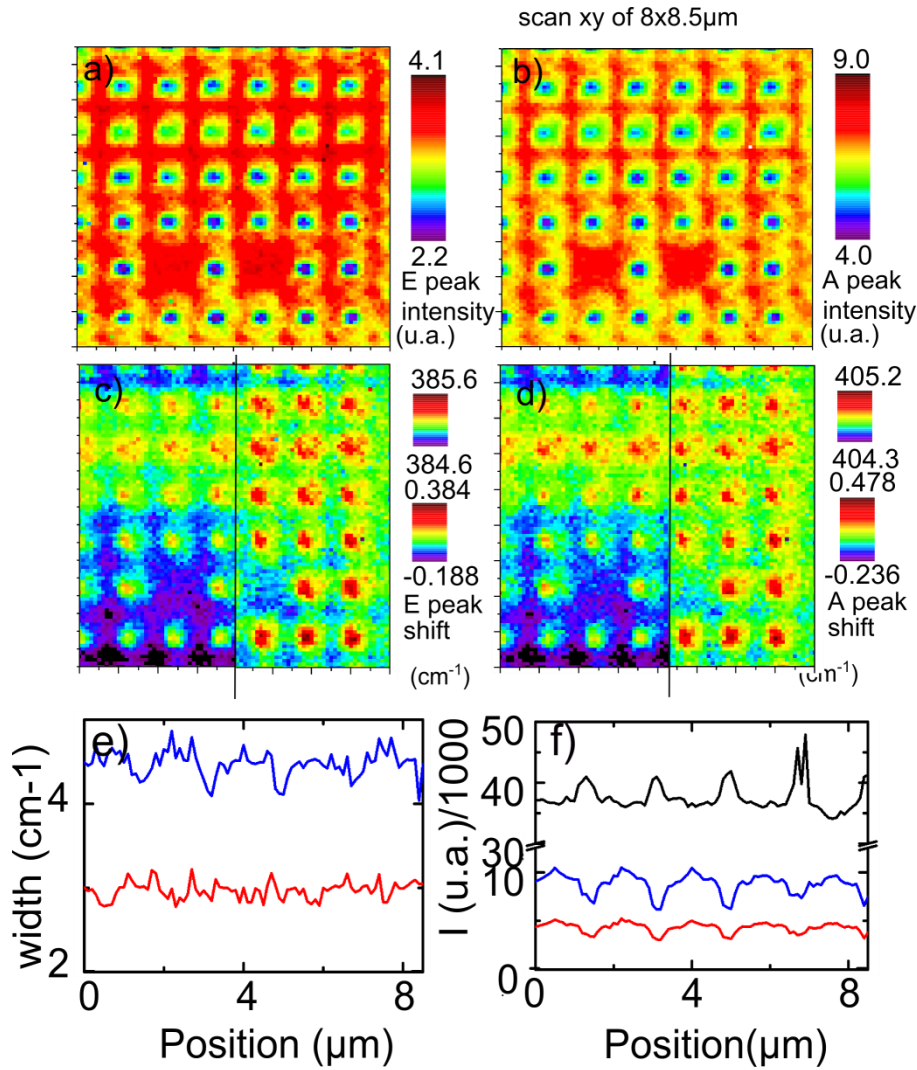


Figure S4b: Figure 1c sample: additional data. A) to d) Raman mapping characterization with peak intensity and position modulation along the sample. We observed a correlation between pillar position and peak modulation. c) and d) we removed, on the right part, a background deviation due to 15 hours of measurements which does not appear in a fast measurement at the exact same position as in e, f, and Figure 3a. e) and f) the peak width and intensity of the sample. We observed a modulation of the A_{1g} peak width with peak appearance which is certainly due to the doping signature and MoS_2 modulation along the pillars. As a first approximation, in the linear variation, we do not expect the heat and strain to affect the width of the A_{1g} peak alone.

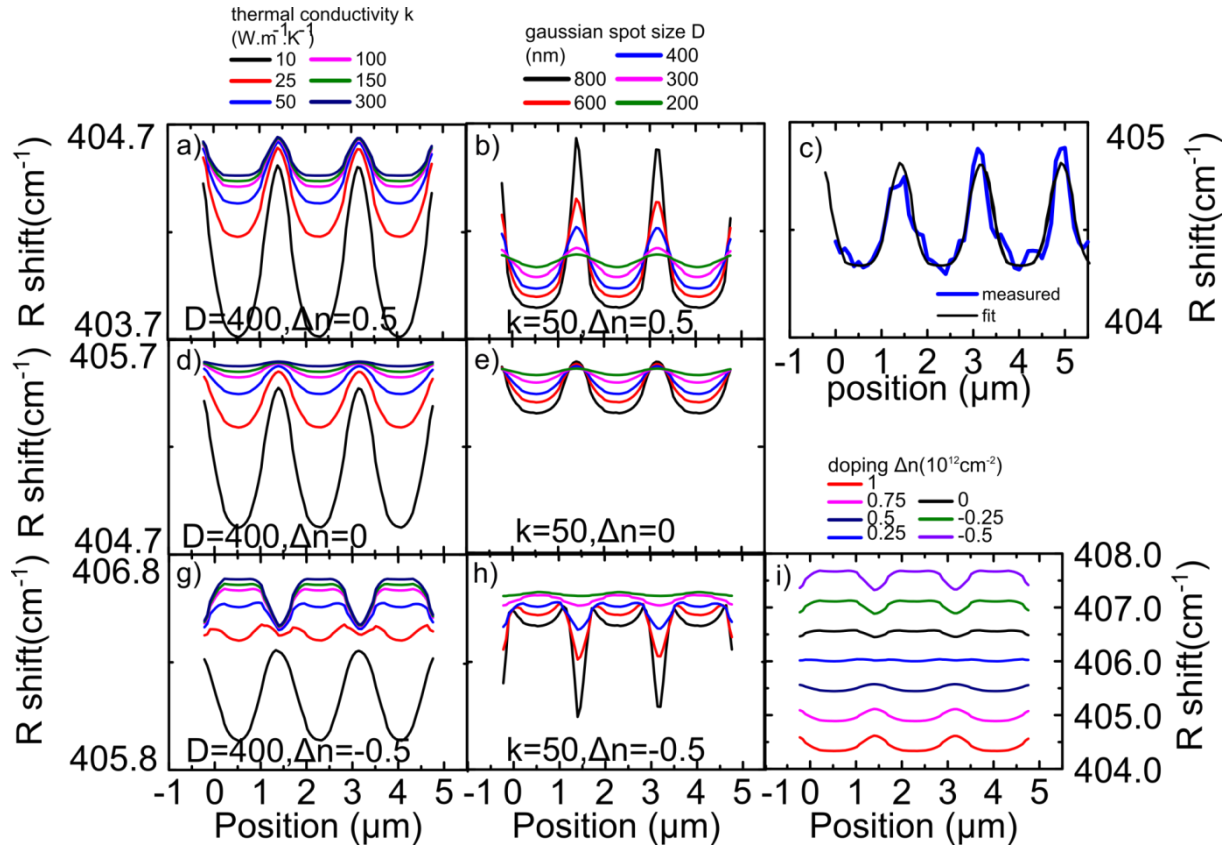


Figure S4c: Figure 1c sample: additional simulation with doping and heating. We used by default the best parameters for the best fit; the doping difference $\Delta n=0.5 \cdot 10^{12} \text{ cm}^{-2}$, the thermal conductivity $k=50 \text{ W} \cdot \text{m}^{-1} \cdot \text{K}^{-1}$, and the Gaussian spot size $D=400 \text{ nm}$. The data and the best fit are shown in c). In the other panel, we have modified one of the parameters; in a), d), g), thermal conductivity, in b), e) and h), Gaussian spot size and in i), doping difference. In a) and b), d) and e), g), and h), we fixed doping values of -0.5 , 0 and 0.5 ($\cdot 10^{12} \text{ cm}^{-2}$), respectively. It is interesting to note that, in d) and e), we have the result without taking into account the doping effect and this is not sufficient to explain the specific shape of our data.

For the COMSOL simulation, presented in Figures 3a and b, of the thermal heat transport in MoS₂, we used:

- density of 2163 e-6 kg/m^3 ,
- heat capacity of 138 J/K/kg ,
- absorption coefficient of 6% per layer.
- number of layers=1
- layer thickness of 1.12 nm
- laser power of $50 \mu\text{W}$ with a 2D Gaussian distribution.

S5: MoS₂ on pillars: the optical cavity created between MoS₂ and SiO₂

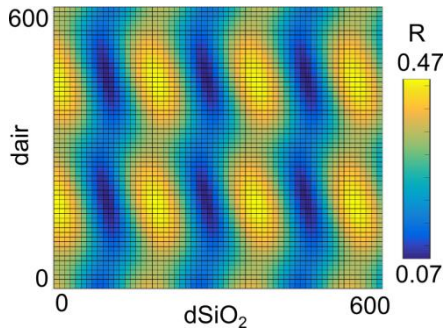


Figure S5: Reflection of the laser modulated by the air cavity distance and SiO₂ thickness.

We simulated the reflection of our system. We defined d_{air} to be the distance between the MoS₂ monolayer and the SiO₂/Si substrate and d_{SiO_2} the thickness of SiO₂. Calculated with the MATLAB Multidiel2 function.

For the Raman and photoluminescence measurements, the reflectance amplitude is modulated by the cavity created between the MoS₂ and the substrate. The space between MoS₂ and the substrate, d_{air} , can be seen as an optical cavity, a very poor one, but an optical cavity all the same and that influences strongly the laser reflection at 532nm. The signal will oscillate between minimum and maximum values, with respect to some periods in d_{air} . In any case, because the cavity is quite poor, it will not enhance the signal on the suspended part drastically for any d_{air} values and does not, by itself, explain the emergence of a strong signal between 1.3 and 1.6eV in Figure 2.

These modulations are important for samples where this distance d_{air} varies a lot, as for the “tent structures”. d_{air} goes from 800nm to 0 in less than 1 μm . In order to determine the laser reflection with accuracy at any position, we simulated the reflectance of a laser at 532nm on a sample made from one monolayer of MoS₂, an air thickness d_{air} , a SiO₂ layer of thickness d_{SiO_2} and a Si substrate. We used a model described in ref ²⁵ to plot the reflectance as a function of d_{air} and d_{SiO_2} . The reflectance is periodic, with both parameters having high amplitudes of oscillation from 47% to 7%.

Nevertheless, in Figure 2, d_{air} can change from 600-800nm to 0 in almost 0.5 μm laterally, along x. This is almost the laser spot size. As mentioned previously, the laser is of a

Gaussian spot size with a diameter around 400nm at best. this means the cavity effect and the fast modulation (2 periods in Figure S5) are completely smoothed out over the sample and we measured an average value which corresponded to a value without any cavity modulation in these “tent “structures. For other samples, this effect can be important in case of bending or any curvature of the MoS₂.

S6: Optomechanics on a network of mechanical resonators with MOS₂ membranes deposited on pillars

Within our MoS₂ samples, mechanical resonators at some positions are basically defined by the pillars near this position. This means that they are defined by 4 pillars for the small resonator and 8 for the large resonators (membranes where a pillar is missing in the middle). It is possible to simulate the motion and resonance frequencies with finite element analyses, but we used a simpler analytical model by approximating our resonator to a circular drum resonator.

We used the Euler Bernoulli model of a membrane to solve the resonance frequency f_0 , as clearly described in ref ²⁶ for a drum;

$$f_0 = \frac{kd}{4\pi} \cdot \sqrt{\frac{16D}{\rho d^4} \cdot \left[\left(\frac{kd}{2} \right)^2 + \frac{\gamma d^2}{4D} \right]}$$

With $D = \frac{Et^3}{12(1-\nu^2)}$, $E=0.33$ Tpa, the Young modulus of the material, $\nu = 0.125$ the Poisson ratio, d the diameter of the membrane, $kd/2 \sim 2.4048$ a coefficient related to geometry, γ the strain, $\rho = 3073$ kg.m⁻² the 2D mass density, and $t=6,15 \cdot 10^{-10}$ m, the monolayer thickness.

The result is described in Figure 5b and fits our data well for a strain between 0.035% and 0.055% (grey area). This means our sample resonances are dominated by the strain, with a spring constant around 0.6 N/m.

S7: MoS₂ on substrate: Raman calibration of heating and doping

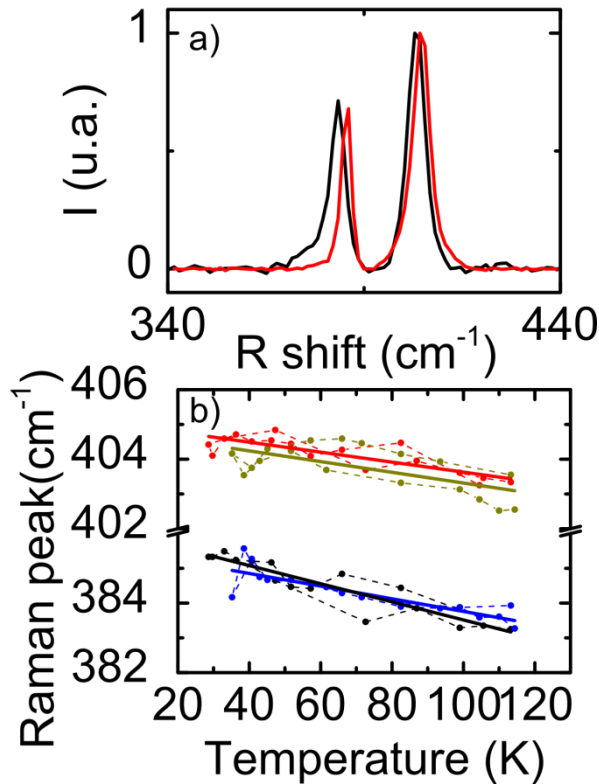


Figure S7a: Calibration of the Raman spectrum in function of the temperature. We have measured the spectrum of different flake of monolayer MoS₂ in function of the temperature directly on the growth substrate of SiO₂/Si. a) Raman spectrum for 30°C (red) and 113°C (black). b) Raman peak position of the A_{1g} and E_{12g} peak position in function of the Temperature with the thermistor at two different places on the hot plate and with back and forth measurements in temperature.

To confirm the quantitative analyze of the thermal conductivity, we did a temperature-Dependent Raman Studies for both E_{12g} and A_{1g} peak dependence. In figure S7b, we measured a $\Delta A_{1g} / \Delta E_{12g}$ ratio of $-0.014 \text{ cm}^{-1} / \text{K}$ and $-0.015 \text{ cm}^{-1} / \text{K}$ for the A_{1g} peak and $-0.018 \text{ cm}^{-1} / \text{K}$ and $-0.026 \text{ cm}^{-1} / \text{K}$ for the E_{12g} peak. For the A_{1g} peak these value are both comparable with previous results in the literature ($-0.016 \text{ cm}^{-1} / \text{K}$).^{11,19} For the E_{12g} peak, we can see a deviation from previous results measured at $-0.013 \text{ cm}^{-1} / \text{K}$ and with our measurements of heating in function of the laser power (see part S4). This small difference can be explain by an additional strain in our sample considering the different flake of MoS₂ used for both measurements; We attribute this strain to the thermal expansion of both layer-substrate system and from different mechanical coupling with the substrate: this is different if the flake stick to the substrate or slide

on the substrate (thermal expansion of monolayer TMDs is 1.10^{-5}K^{-1} and of Si is 2.10^{-6}K^{-1} ; for 100°C , it can eventually modify the length of the flake by 1% depending of the coupling nature with the substrate). Our measurements were done at ambient conditions with a TH10K thermistor and HT24S ceramic heater from Thorlab and decouple with Kapton layer and a Teflon plate (Figure S7c). We took care to work at the exact same position between each point and to stabilize the temperature of the system with sufficiently long time scale. To confirm our temperature measurements, we have done two measurements, on two different MoS_2 flakes. Each time, we have placed the thermal coupler at two different places on the heater (brown and red curve in S7b for example) and we have not seen any notable difference in the A^1_g peak dependence. We have measured with $P=100\mu\text{W}$ in order to be sure of the absence of heating from the laser itself.

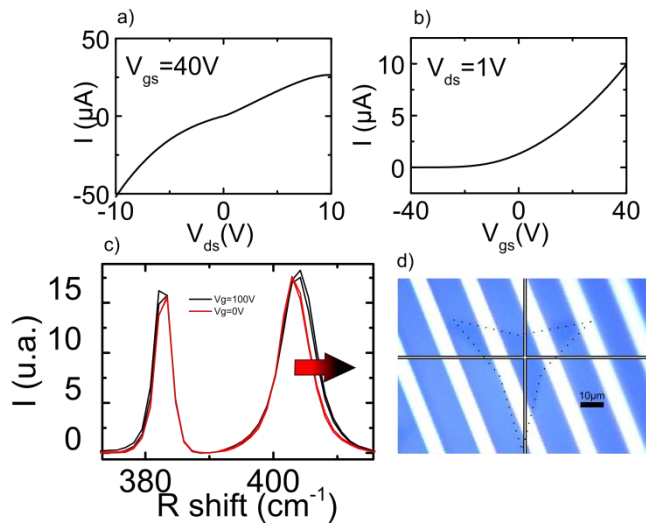


Figure S7b: Calibration of the Raman spectrum in function of the doping for a MoS_2 flake on SiO_2/Si substrate. a) and b) we have measured the $I(V)$ curve with a probe station. c) An image of the set-up under Raman spectrum. d) An image of the MoS_2 flake under test connected to interdigitated metallic pads. The crossbar indicates the laser position. e) Raman spectrum of MoS_2 with different gate voltage of 0 and 100V at ambient conditions with a laser power of $100\mu\text{W}$. We observe a shift of the peak and a broadening with doping. We proceeded twice to the same measurement and we have seen the good reproducibility of our results.

We have also done some Raman spectrum measurement of our MoS_2 under different electrical polarization in order to calibrate the Raman doping dependence and confirm our statement on this point. We have contacted, by e-beam lithography, a MoS_2 flake on a substrate with interdigitated gold pads with the substrate acting as a bottom back gate. The dielectric thickness

is 300nm and the gate capacitance C_g is $8.9\text{nF}\cdot\text{cm}^{-2}$. We have measured the I-V characteristic with a probe station and an Agilent 4155C at ambient conditions under white light illumination. The MoS₂ is naturally n-doped with the Fermi level closed to the semiconducting band gap. We have proceeded with Raman measurements at different gate voltage (with a Keithley 228A). We measure an upshift of the A^1_g peak of 0.7cm^{-1} with a broadening of the peak between $V_g=0\text{V}$ and $V_g=100\text{V}$. On contrary the $E^{1_{2g}}$ peak is not affected by doping. All these behaviors are expected for doping variation if we consider the value measured in the literature of 2.2cm^{-1} for A^1_g peak and a doping shift of 10^{13}cm^{-2} . Our shift corresponds to a doping change of $3\cdot 10^{12}\text{cm}^{-2}$. If we consider the relation between charge density and the capacitance $n\cdot e=C_g\cdot\Delta V_g$ with e the electron charge= $1.6\cdot 10^{-19}\text{C}$ and ΔV_g the gate shift, we can estimate the doping change to be around $5\cdot 10^{12}\text{cm}^{-2}$; not very far from the measured value. We confirm our data analyses through this calibration.

SOM References

- (1) Reserbat-Plantey, A.; Kalita, D.; Han, Z.; Ferlazzo, L.; Autier-Laurent, S.; Komatsu, K.; Li, C.; Weil, R.; Ralko, A.; Marty, L.; Guéron, S.; Bendiab, N.; Bouchiat, H.; Bouchiat, V. Strain Superlattices and Macroscale Suspension of Graphene Induced by Corrugated Substrates. *Nano Lett.* **2014**, *14*, 5044–5051.
- (2) Palacios-Berraquero, C.; Kara, D. M.; Montblanch, A. R.-P.; Barbone, M.; Latawiec, P.; Yoon, D.; Ott, A. K.; Loncar, M.; Ferrari, A. C.; Atatüre, M. Large-Scale Quantum-Emitter Arrays in Atomically Thin Semiconductors. *Nat. Commun.* **2017**, *8*, 15093.
- (3) Branny, A.; Kumar, S.; Proux, R.; Gerardot, B. D. Deterministic Strain-Induced Arrays of Quantum Emitters in a Two-Dimensional Semiconductor. *Nat. Commun.* **2017**, *8*, 15053.
- (4) Lloyd, D.; Liu, X.; Christopher, J. W.; Cantley, L.; Wadehra, A.; Kim, B. L.; Goldberg, B. B.; Swan, A. K.; Bunch, J. S. Band Gap Engineering with Ultralarge Biaxial Strains in Suspended Monolayer MoS₂. *Nano Lett.* **2016**, *16*, 5836–5841.
- (5) Li, H.; Contryman, A. W.; Qian, X.; Ardakani, S. M.; Gong, Y.; Wang, X.; Weisse, J. M.; Lee, C. H.; Zhao, J.; Ajayan, P. M.; Li, J.; Manoharan H.C.; Zheng, X. Optoelectronic Crystal of Artificial Atoms in Strain-Textured Molybdenum Disulphide. *Nat. Commun.* **2015**, *6*, 7381.

- (6) Rice, C.; Young, R. J.; Zan, R.; Bangert, U.; Wolverson, D.; Georgiou, T.; Jalil, R.; Novoselov, K. S. Raman-Scattering Measurements and First-Principles Calculations of Strain-Induced Phonon Shifts in Monolayer MoS₂. *Phys. Rev. B* **2013**, *87*, 081307.
- (7) Conley, H. J.; Wang, B.; Ziegler, J. I.; Haglund, R. F.; Pantelides, S. T.; Bolotin, K. I. Bandgap Engineering of Strained Monolayer and Bilayer MoS₂. *Nano Lett.* **2013**, *13*, 3626–3630.
- (8) McCreary, A.; Ghosh, R.; Amani, M.; Wang, J.; Duerloo, K.-A. N.; Sharma, A.; Jarvis, K.; Reed, E. J.; Dongare, A. M.; Banerjee, S. K.; Terrones, M.; Namburu, R.R.; Dubey, M. Effects of Uniaxial and Biaxial Strain on Few-Layered Terrace Structures of MoS₂ Grown by Vapor Transport. *ACS Nano* **2016**, *10*, 3186–3197.
- (9) Wang, Y.; Cong, C.; Qiu, C.; Yu, T. Raman Spectroscopy Study of Lattice Vibration and Crystallographic Orientation of Monolayer MoS₂ under Uniaxial Strain. *Small* **2013**, *9*, 2857–2861.
- (10) Chakraborty, B.; Bera, A.; Muthu, D. V. S.; Bhowmick, S.; Waghmare, U. V.; Sood, A. K. Symmetry-Dependent Phonon Renormalization in Monolayer MoS₂ Transistor. *Phys. Rev. B* **2012**, *85*, 161403.
- (11) Lanzillo, N. A.; Glen Birdwell, A.; Amani, M.; Crowne, F. J.; Shah, P. B.; Najmaei, S.; Liu, Z.; Ajayan, P.M.; Lou, J.; Dubey, M.; Nayak, S. K.; Nayak, S. K. Temperature-Dependent Phonon Shifts in Monolayer MoS₂. *Appl. Phys. Lett.* **2013**, *103*, 093102.
- (12) Yan, W.; He, W.-Y.; Chu, Z.-D.; Liu, M.; Meng, L.; Dou, R.-F.; Zhang, Y.; Liu, Z.; Nie, J.-C.; He, L. Strain and Curvature Induced Evolution of Electronic Band Structures in Twisted Graphene Bilayer. *Nat. Commun.* **2013**, *4*.
- (13) He, K.; Poole, C.; Mak, K. F.; Shan, J. Experimental Demonstration of Continuous Electronic Structure Tuning via Strain in Atomically Thin MoS₂. *Nano Lett.* **2013**, *13*, 2931–2936.
- (14) Zhu, C. R. Strain Tuning of Optical Emission Energy and Polarization in Monolayer and Bilayer MoS₂. *Phys. Rev. B* **2013**, *88*.
- (15) Steinhoff, A.; Kim, J.-H.; Jahnke, F.; Rösner, M.; Kim, D.-S.; Lee, C.; Han, G. H.; Jeong, M. S.; Wehling, T. O.; Gies, C. Efficient Excitonic Photoluminescence in Direct and Indirect Band Gap Monolayer MoS₂. *Nano Lett.* **2015**, *15*, 6841–6847.
- (16) Mak, K. F.; He, K.; Lee, C.; Lee, G. H.; Hone, J.; Heinz, T. F.; Shan, J. Tightly Bound Trions in Monolayer MoS₂. *Nat. Mater.* **2013**, *12*, 207–211.

- (17) Scheuschner, N.; Ochedowski, O.; Kaulitz, A.-M.; Gillen, R.; Schleberger, M.; Maultzsch, J. Photoluminescence of Freestanding Single- and Few-Layer MoS_2 . *Phys. Rev. B* **2014**, *89*, 125406.
- (18) Castellanos-Gomez, A.; Roldán, R.; Cappelluti, E.; Buscema, M.; Guinea, F.; van der Zant, H. S. J.; Steele, G. A. Local Strain Engineering in Atomically Thin MoS_2 . *Nano Lett.* **2013**, *13*, 5361–5366.
- (19) Sahoo, S.; Gaur, A. P. S.; Ahmadi, M.; Guinel, M. J.-F.; Katiyar, R. S. Temperature-Dependent Raman Studies and Thermal Conductivity of Few-Layer MoS_2 . *J. Phys. Chem. C* **2013**, *117*, 9042–9047.
- (20) Buscema, M.; Steele, G. A.; Zant, H. S. J. van der; Castellanos-Gomez, A. The Effect of the Substrate on the Raman and Photoluminescence Emission of Single-Layer MoS_2 . *Nano Res.* **2014**, *7*, 561–571.
- (21) Lee, J. E.; Ahn, G.; Shim, J.; Lee, Y. S.; Ryu, S. Optical Separation of Mechanical Strain from Charge Doping in Graphene. *Nat. Commun.* **2012**, *3*, 1024.
- (22) Kim, I. S.; Sangwan, V. K.; Jariwala, D.; Wood, J. D.; Park, S.; Chen, K.-S.; Shi, F.; Ruiz-Zepeda, F.; Ponce, A.; Jose-Yacamán, M.; Dravid, V. P.; Marks, T. J.; Hersam, M. C.; Lauhon, L. J. Influence of Stoichiometry on the Optical and Electrical Properties of Chemical Vapor Deposition Derived MoS_2 . *ACS Nano* **2014**, *8*, 10551–10558.
- (23) Pierucci, D.; Henck, H.; Avila, J.; Balan, A.; Naylor, C. H.; Patriarche, G.; Dappe, Y. J.; Silly, M. G.; Sirotti, F.; Johnson, A. T. C.; Asensio, M. C.; Ouerghi, A. Band Alignment and Minigaps in Monolayer MoS_2 -Graphene van Der Waals Heterostructures. *Nano Lett.* **2016**, *16*, 4054–4061.
- (24) Henck, H.; Pierucci, D.; Chaste, J.; Naylor, C. H.; Avila, J.; Balan, A.; Silly, M. G.; Asensio, M. C.; Sirotti, F.; Johnson, A. T. C.; Lhuillier, E.; Ouerghi, A. Electrolytic Phototransistor Based on Graphene- MoS_2 van Der Waals p-n Heterojunction with Tunable Photoresponse. *Appl. Phys. Lett.* **2016**, *109*, 113103.
- (25) Wang, Z.; Feng, P. X.-L. Interferometric Motion Detection in Atomic Layer 2D Nanostructures: Visualizing Signal Transduction Efficiency and Optimization Pathways. *Sci. Rep.* **2016**, *6*, 28923.
- (26) Lee, J.; Wang, Z.; He, K.; Shan, J.; Feng, P. X.-L. High Frequency MoS_2 Nanomechanical Resonators. *ACS Nano* **2013**, *7*, 6086–6091.